Monthly Notices
of the
ROYAL ASTRONOMICAL SOCIETY
MNRAS **456,** 3296–3317 (2016) doi:10.1093/mnras/stv2811

The spectacular evolution of Supernova 1996al over 15 yr: a low-energy explosion of a stripped massive star in a highly structured environment

S. Benetti,[1⋆] N. N. Chugai,[2] V. P. Utrobin,[3] E. Cappellaro,[1⋆] F. Patat,[4] A. Pastorello,[1] M. Turatto,[1] G. Cupani,[5] R. Neuhäuser,[6] N. Caldwell,[7] G. Pignata[8,9] and L. Tomasella[1]

[1]*INAF – Osservatorio Astronomico di Padova, vicolo dell'Osservatorio 5, I-35122 Padova, Italy*
[2]*Institute of Astronomy of Russian Academy of Sciences, Pyatnitskaya St 48, 119017 Moscow, Russia*
[3]*Institute of Theoretical and Experimental Physics, B. Cheremushkinskaya St 25, 117218 Moscow, Russia*
[4]*European Southern Observatory, Karl-Schwarzschild-Str. 2, D-85748 Garching bei München, Germany*
[5]*INAF – Osservatorio Astronomico di Trieste, Via G.B. Tiepolo, 11, I-34131 Trieste, Italy*
[6]*Astrophysikalisches Institut und Universitäts-Sternwarte, FSU Jena, Schillergäßchen 2-3, D-07745 Jena, Germany*
[7]*Harvard–Smithsonian Center for Astrophysics, Cambridge, MA 02138, USA*
[8]*Departamento de Ciencias Fisicas, Universidad Andres Bello, Avda. Republica 252, Santiago, Chile*
[9]*Millennium Institute of Astrophysics, Chile*

Accepted 2015 November 27. Received 2015 November 26; in original form 2015 September 22

ABSTRACT

Spectrophotometry of SN 1996al carried out throughout 15 yr is presented. The early photometry suggests that SN 1996al is a linear Type II supernova, with an absolute peak of $M_V \sim -18.2$ mag. Early spectra present broad asymmetric Balmer emissions, with superimposed narrow lines with P-Cygni profile, and He I features with asymmetric broad emission components. The analysis of the line profiles shows that the H and He broad components form in the same region of the ejecta. By day +142, the Hα profile dramatically changes: the narrow P-Cygni profile disappears, and the Hα is fitted by three emission components that will be detected over the remaining 15 yr of the supernova (SN) monitoring campaign. Instead, the He I emissions become progressively narrower and symmetric. A sudden increase in flux of all He I lines is observed between 300 and 600 d. Models show that the SN luminosity is sustained by the interaction of low-mass ($\sim$1.15 $M_\odot$) ejecta, expelled in a low kinetic energy ($\sim 1.6 \times 10^{50}$ erg) explosion, with highly asymmetric circumstellar medium. The detection of Hα emission in pre-explosion archive images suggests that the progenitor was most likely a massive star ($\sim$25 $M_\odot$ ZAMS) that had lost a large fraction of its hydrogen envelope before explosion, and was hence embedded in a H-rich cocoon. The low-mass ejecta and modest kinetic energy of the explosion are explained with massive fallback of material into the compact remnant, a 7–8-$M_\odot$ black hole.

Key words: supernovae: general.

1 INTRODUCTION

The aftermath of a supernova (SN) explosion is a bubble of gas expanding at very high velocity. Eventually, the ejecta may impact on the pre-existing circumstellar material (CSM), generating a shock in which a fraction of the kinetic energy of the ejecta is converted into radiation. The intensity of the resulting emission mostly depends on the density of the CSM and the velocity contrast between the ejecta and the CSM. If the density of the CSM is low, the emission from the CSM–ejecta interaction becomes visible only after the SN luminosity has faded, sometimes several years after the explosion. However, occasionally, the CSM near the SN is so dense that the CSM–ejecta interaction dominates the SN emission even at early phases.

With improved statistics and quality of observations, we are now observing counterparts for the different scenarios, and a new taxonomy for Type II supernovae (SNII), based on the mass of the residual hydrogen envelope and the strength of the CSM–ejecta

⋆E-mail: stefano.benetti@oapd.inaf.it (SB); enrico.cappellaro@oapd.inaf.it (EC)

interaction signatures, can be proposed. The emission of classical SNII is determined by the thermal balance in the ejecta, and CSM–ejecta interaction is negligible (at least at early phases). Depending on the shape of the light curve, they are sub-classified into plateau (IIP) and linear (IIL) types. The current interpretation is that different light curves correspond to different envelope masses, ranging from $\sim$10 $M_\odot$ in SNIIP (cf. Smartt 2009) to $\sim$1 $M_\odot$ in SNIIL, due to different progenitor initial masses and mass-loss histories. When soon after the explosion the SN ejecta interact with a dense CSM, the SN emission itself is overwhelmed by the emission arising from the interaction (Chugai 1990; Chevalier & Fransson 1994; Terlevich 1994). Best examples of this class are SN 1988Z (Turatto et al. 1993; Aretxaga et al. 1999), with a long plateau-like light curve, and SN 1998S (Fassia et al. 2000; Liu et al. 2000) with a linear-like light curve. These SNe are named as Type IIn.

In some SNII, the CSM–ejecta interaction contribution emerges only when the ^{56}Co decay energy input fades. The fact that these are mostly SNIIL is consistent with our understanding that they experienced stronger mass-loss during their evolutions (e.g. SNe 1980K, 1979C, and 1990K; Uomoto & Kirshner 1986; Fesen et al. 1999; Cappellaro et al. 1995, respectively), hence they are expected to have higher CSM density.

Somewhat in between, a few SNe have emission line profiles which reveal the presence of a CSM around the exploding stars from early-on, though the ejecta–CSM interaction becomes preponderant some months later. These are sometimes labelled SNIId, where 'd' stands for 'double' profile because of the simultaneous presence of broad profiles from the ejecta and narrow ones from the CSM. SN 1994aj (Benetti et al. 1998, Paper I) and SN 1996L (Benetti et al. 1999, Paper II) belong to this group.

In this paper we present the study of a new SN (SN 1996al) with spectroscopic properties very similar to those of SNIId (Benetti & Neuhauser 1996). SN 1996al was visually discovered on July 22.71 UT by Evans et al. (1996), about 30 arcsec north of the centre of its host galaxy, NGC 7689. The measured position of the SN is RA = $23^h33^m16^s.29 \pm 0.03$; Dec. = $-54°04'59''.69 \pm 0.05$ (J2000.0), in agreement with that reported by Evans et al. (1996).

In view of its relative closeness and apparent brightness, an extensive observational campaign was set up with the European Southern Observatory (ESO)-Chile telescopes. Thanks to this massive effort, we have been able to follow the SN for more than 15 yr, and it has become one of the best monitored SNIIL–SNIId.

In this paper we will describe the physical properties of the explosion and constrain the nature of SN 1996al progenitor star.

2 OBSERVATIONS

Spectroscopy and imaging observations were carried out at ESO La Silla and Paranal Observatories using a number of different telescopes and/or instruments (see Tables A1 and A2).

2.1 Optical photometry

The CCD frames were first bias and flat-field corrected in a standard manner. Since a fraction of data was obtained under non-photometric conditions, relative photometry was performed with respect to a local sequence of field stars (see Fig. 1). 12 photometric nights were used to calibrate this sequence against Landolt standard stars (Landolt 1992). The magnitudes and estimated errors of the local standards are shown in Table 1. These magnitudes were obtained by summing the counts through an aperture, whose size varied according to the seeing.

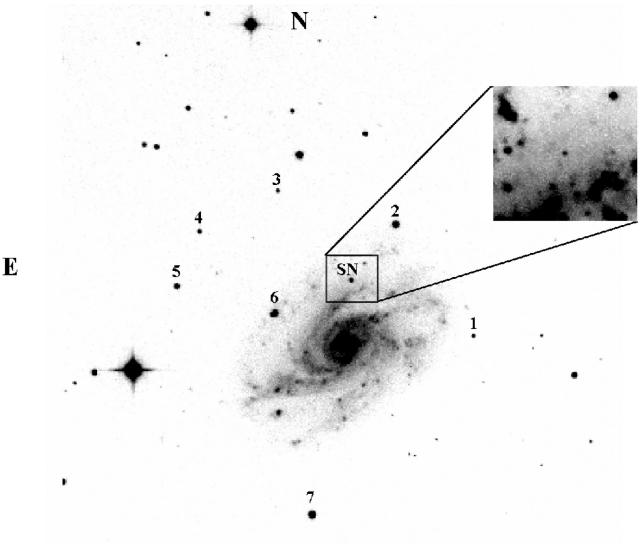

Figure 1. SN 1996al in NGC 7689 and reference stars. The main image is an *R* frame taken on 1996 October 1 with the D1.54m+DFOSC. The seeing is 1.4 arcsec and the field of view is 5.9 arcsec × 5.9 arcsec. The zoomed image was obtained with VLT+FORS2 using a redshifted H α filter on 2002 June 16. The seeing was 0.7 arcsec and the field of view is 25 arcsec. The SN is the source at the centre of the image.

Table 1. Magnitudes of the local sequence stars as identified in Fig. 1.

Star	*U*	*B*	*V*	*R*	*I*
1	20.36(06)	19.33(03)	18.27(02)	17.60(03)	17.06(03)
2[a]	15.67(03)	15.84(03)	15.45(02)	15.16(02)	14.89(02)
3	21.26(11)	19.98(04)	18.52(02)	17.58(03)	16.67(03)
4	18.77(04)	18.37(05)	17.58(03)	17.09(03)	16.63(02)
5	20.37(10)	19.18(05)	17.68(03)	16.37(03)	14.89(03)
6[b]	17.67(05)	17.00(05)	16.11(03)	15.53(04)	15.05(03)
7	15.70(02)	15.61(02)	15.00(02)	14.63(03)	14.31(03)

Notes. [a]For this star we have also IR magnitudes: $J = 14.55(03)$, $H = 14.18(03)$, $K = 14.28(03)$. [b]Double star: magnitudes refer to the brighter component.

Ideally, one would like to remove the galaxy background by subtracting a galaxy 'template' where the SN is absent. However, a suitable template image was not available. Therefore, the SN magnitudes were measured using the IRAF[1] point spread function (PSF) fitting task Daophot (Stetson 1992) and/or ROMAFOT package (Buonanno et al. 1983) under MIDAS.[2] These procedures allowed the simultaneous fit and subtraction of the galaxy background. While the pixel scales changed from one instrument to another, they were always sufficiently small to provide good sampling of the PSF (see last column, and caption of Table A1). The SN magnitudes with estimated internal errors are listed in Table A1, which also gives the seeing for each epoch, averaged over the observed bands.

On 2007 December 8, an Hα frame of SN 1996al was also secured with VLT+FORS2, and the frame was calibrated observing in the same night the spectrophotometric standard G158-100 (Oke 1990).

[1] IRAF is distributed by the National Optical Astronomy Observatories, which are operated by the Association of Universities for Research in Astronomy, Inc., under cooperative agreement with the National Science Foundation.
[2] https://www.eso.org/sci/software/esomidas/

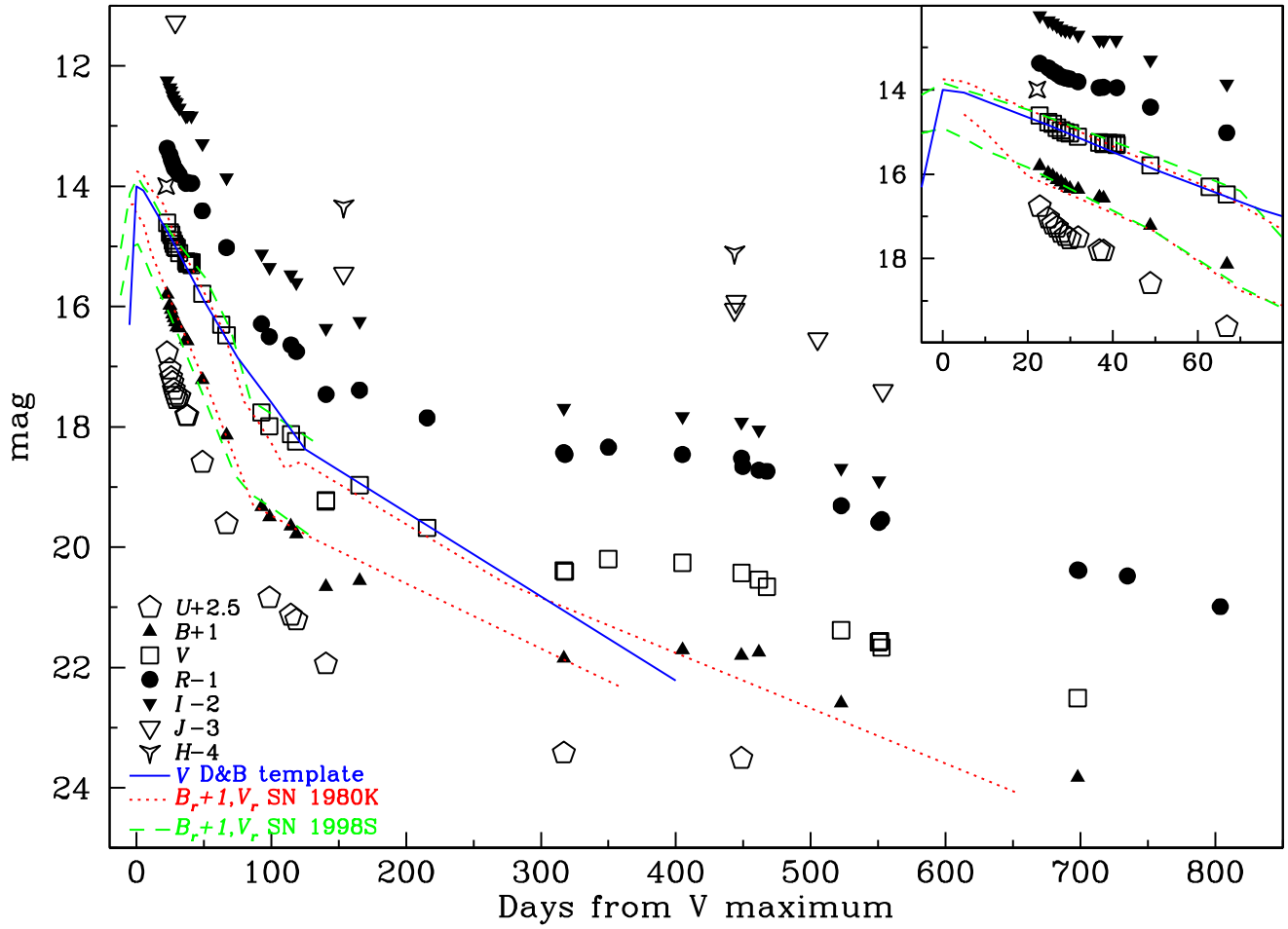

Figure 2. *U*, *B*, *V*, *R*, *I*, *J* and *H* light curves of SN 1996al. The dotted lines represent the *B* and *V* light curves of SN 1980K (Barbon, Ciatti & Rosino 1982; Buta 1982; Tsvetkov 1983). The distance to the SN 1980K host galaxy, NGC 6948, is taken from Karachentsev, Sharina & Huchtmeier (2000). The SN 1980K *B*, *V* light curves are reported to the distance and reddening of SN 1996al with a +0.3 mag shift, and labelled B_r and V_r in the figure. The dashed lines represent the *B* and *V* light curves of SN 1998S (Fassia et al. 2000; Liu et al. 2000). The distance for the SN 1998S host galaxy, NGC 3877, is taken from Willick et al. (1997). The SN 1998S *B*, *V* light curves are reported to the distance and reddening of SN 1996al with a +1.5 mag shift, and labelled B_r and V_r in the figure. The starry symbol is the visual SN estimate at the discovery from Evans et al. (1996). The best match with the template *V* light curve of SNIIL (from Doggett & Branch 1985), along with the comparisons with those of SNe 1980K and 1998S, suggest that the maximum occurred on MJD ∼50265 ± 2 d at a magnitude $V \sim 13.9 \pm 0.3$.

The derived Hα flux inside the SN 1996al PSF was found to be in excellent agreement with that derived from the subsequent FORS2 spectrum (Section 2.4).

2.1.1 *Light curves*

The *UBVRIJH* light curves are plotted in Fig. 2.

Patat et al. (1994) showed that SNII can be characterized on the basis of the β_{100} parameter, which quantifies the luminosity decline rate in the first 100 d after maximum light. For SN 1996al, we measure $\beta^{\rm B}_{100} = 4.84$ mag (100 d)$^{-1}$, which is typical of the Type IIL sub-class, very similar for instance to SN 1980K. However, the post-maximum decline shows a short plateau-like break (see inset of Fig. 2) in all bands. This flattening is reached at day +30 in *U* and *B* bands, and is very short (2–3 d). In *VRI* it is reached a few days later (+34 d), and it lasts about one week.

The comparisons with the light curves of SNe 1980K and 1998S *V*, and the *V*-band template light curve of SNIIL from Doggett & Branch (1985), suggest that SN 1996al reaches the *V* maximum on MJD = 50265 ± 2 (1996 June 30), i.e. 23 d prior to our first observation, and likely with a *V* peak magnitude of about 13.9 ± 0.3 ($B = 13.7 \pm 0.3$). In the following, we will adopt this estimate of the *V* maximum epoch as reference time. The epoch of the *B*-band peak is coincident with that of the *V* maximum. However, we stress that these estimates are subject to relatively large uncertainty, since the maxima themselves were not observed and SNIIL show a variety of photometric behaviours around the maximum epochs (Faran et al. 2014). In Table 2, the main parameters of the *UBVRI* light curves of SN 1996al are summarized.

An inflection point in the linear decline is observed at about day +150. Between +150 and about +320 d the light curves, though not well sampled, show declines that match the ^{56}Co decay rate [0.98 mag (100 d)$^{-1}$; Table 2]. From +320 to +450 d the light curves level out to a new plateau, where the *V* light curve slightly increases in luminosity by +0.2 mag, and *R* by ∼+ 0.1 mag. After this plateau, the *BVRIJ* light curves start a monotonic decline (with some modulation in the *R* band) with rates very similar to those observed between 150 and 300 d (Table 2).

Table 2. *UBVRIJ* light-curve parameters.

Band	Post-max decline	Start short plateau from *V*max	Plateau duration	Plateau	Post-plateau decline	Decline (150–300 d)	Decline (>450 d)
	mag (100 d)$^{-1}$	d	d	mag	mag (100 d)$^{-1}$	mag (100 d)$^{-1}$	mag (100 d)$^{-1}$
U	10.73	+30	2	15.01	4.98	≥0.84	
B	7.46	+30	2	15.35	4.85	0.85	0.84
V	5.55[a]	+34	7	15.28	4.65	0.89	0.86
R	5.03	+34	7	14.95	4.38	0.67	0.67
I	5.12	+34	7	14.83	4.31	0.95	0.98
J							1.24

Note. [a]Excluding the visual estimation of Evans et al. (1996).

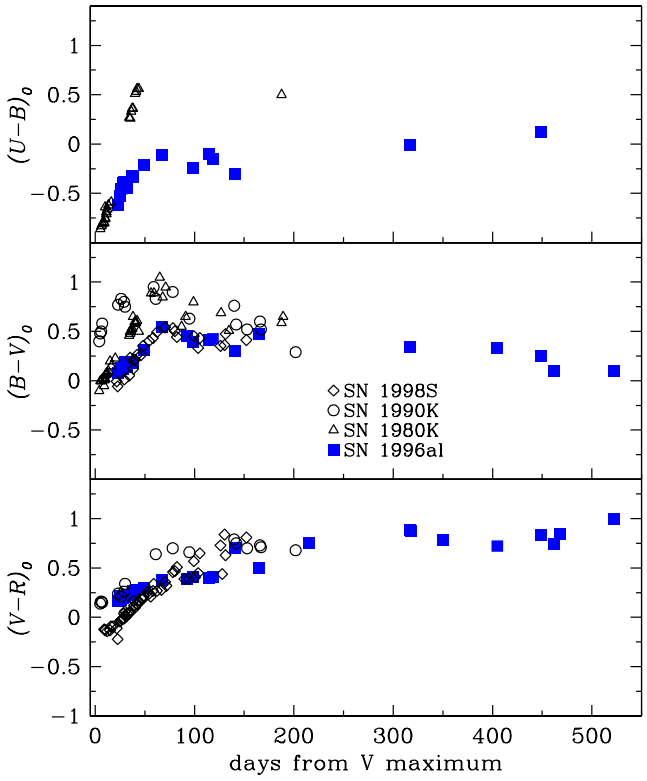

Figure 3. The dereddened colour curves of SN 1996al are compared with those of SN 1980K and SN 1990K (Cappellaro et al. 1995).

2.1.2 *Colour curves*

In Fig. 3, the extinction-corrected[3] $(U-B)_0$, $(B-V)_0$ and $(V-R)_0$ colour curves of SN 1996al are plotted along with those of two bright SNIIL, SNe 1980K and 1990K, and SN 1998S.

The early $(U-B)_0$ colour curve of SN 1996al is consistent with that of SN 1980K. It shows a smooth increase reaching a value of −0.1 mag at about 70 d. From day +140, it experiences a linear increase from −0.30 to +0.13 mag at phase 450 d, although the colour-curve sampling is poor. However, it never reaches the red colours observed in SN 1980K (+0.5 mag).

The $(B-V)_0$ colour curve shows an overall similar behaviour as the $(U-B)_0$ colour curve. It is initially blue (+0.07 mag), then it smoothly increases to a maximum of +0.54 mag at ∼70 d, followed by a slow decline. At late times, the $(B-V)_0$ colour curve remains substantially constant at +0.34 mag with a small decrease to about 0.24 mag at about 460 d after maximum.

The overall appearance of the $(B-V)$ colour curve is very similar to that of SN 1998S, and not very discrepant from that of SN 1980K, although somehow displaced in phase. Also in this colour, SN 1996al never reaches the red values ($(B-V)\sim1$ mag) shown by SN 1980K. SN 1990K, another bright SNIIL studied by Cappellaro et al. (1995), showed very red colours already at maximum. At phases close to ∼+ 160 d, all four SNe have similar $(B-V)$ colours. Finally, the SN 1996al $(V-R)$ colour curve experiences a gradual 'reddening' with early values similar to those seen in SN 1990K. After +100 d, the $V-R$ colour curves of the two SNe show a plateau-like feature, with a $(V-R)\sim0.41$ mag for SN 1996al. Starting at about day +120, $(V-R)$ further increases to ∼0.9 mag, and remains thereafter almost constant.

2.2 Reddening and distance to NGC 7689

The Galactic reddening towards NGC 7689 is $A_B = 0.051$ mag (Schlegel, Finkbeiner & Davis 1998). The higher signal-to-noise (S/N) ratio spectra of SN 1996al show narrow absorptions due to interstellar Na ID, suggesting that some light extinction may occur within the parent galaxy. The mean equivalent width (EW) of this doublet averaged over 10 measurements is 0.60 ± 0.08 Å. Using the relation $E(B-V) \sim 0.16 \times$ EW (Na ID) of Turatto, Benetti & Cappellaro (2003) yields $E(B-V)_{\rm host} \sim 0.10 \pm 0.05$ mag. In the following, we will adopt for SN 1996al a total reddening of $E(B-V)_{\rm tot} = 0.11 \pm 0.05$ mag.

From the Na ID interstellar lines we also derive a mean recessional velocity of 1835 ± 68 km s^{-1} for NGC 7689, to be compared with the optical (1974 ± 6 km s^{-1}) and radio (1970 ± 5 km s^{-1}) velocities given by NED.[4] The difference (−135 km s^{-1}) is likely due to the host galaxy rotation, projected along the line of sight (LOS).

Adopting a value of $H_0 = 73$ km s^{-1} Mpc^{-1} along with the radio heliocentric radial velocity of 1967 km s^{-1}, and correcting it for Local Group infall on to the Virgo cluster, NED gives for NGC 7689 a distance modulus of $\mu_B = 31.98$ (24.89 Mpc).

On the other hand, using the relative distance of NGC 7689 from the Virgo cluster (of 1.37; Kraan-Korteweg 1986), and assuming a Virgo cluster distance of 15.3 Mpc (Freedman et al. 2001), a distance modulus of $\mu_B = 31.61$ mag (20.96 Mpc) is derived for NGC 7689.

[3] Using the Cardelli, Clayton & Mathis (1989) extinction law, and the reddening value discussed in Section 2.2.

[4] http://ned.ipac.caltech.edu

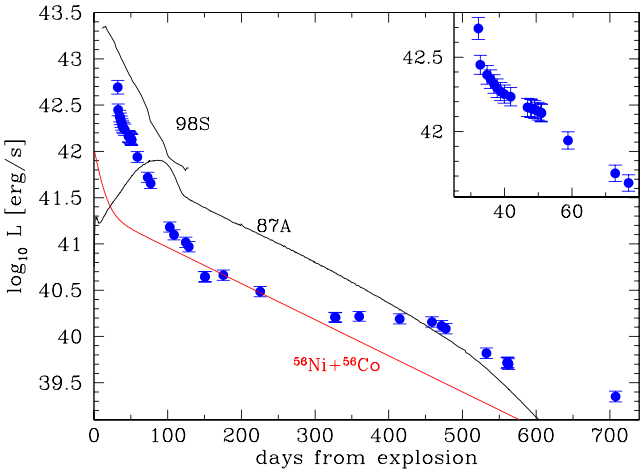

Figure 4. Bolometric *uvoir* light curve of SN 1996al. A zoom of the *uvoir* curve in phases near maximum is shown in the upper-right box. For comparison, the ^{56}Ni+^{56}Co decay model in the hypothesis of full γ-rays trapping is also reported. The rise time to maximum was assumed to be 10 d.

The mean value of the above estimates, $\mu_B = 31.80 \pm 0.20$ mag (22.91 Mpc) is adopted throughout the paper as distance modulus for NGC 7689.

2.3 Absolute magnitudes and bolometric light curve

With the above assumptions for extinction and distance (using the Cardelli et al. 1989, extinction law), we obtain $M_B \sim -18.6 \pm 0.4$ and $M_V \sim -18.2 \pm 0.3$ for the SN absolute B and V magnitudes at maximum. These are similar to those of the 'bright' SNIIL subclass (which have an $<M_B> = -19.0 \pm 0.6$ mag, rescaled to $H_0 = 73$ km s^{-1} Mpc^{-1}; Patat et al. 1994).

In order to compute the energy budget of SN 1996al and to simplify the comparison with theory, it is useful to determine the bolometric light curve. Unfortunately, no observations at UV, X-ray or radio wavelengths are available. We are then limited to derive a pseudo-bolometric (*UBVRIJHK*, or *uvoir*) light curve. This was obtained first adding the *UBVRIJ* contributions and then calculating the *HK* contributions in the phase range 153–408 d, assuming during this period a constant $H - K$ colour. The *HK* contribution resulted in $\log L_{UtoK} - \log L_{UtoJ} = 0.08 \pm 0.01$ dex for this period. We made the assumption that the IR contribution to the total luminosity remained constant at earlier epochs. The bolometric curve shown in Fig. 4 shares all relevant features already noted in chromatic curves: the overall linear decay up to 150 d after explosion, including a hint of a plateau around day +30. It shows a break in the decay at around day +150, then a ^{56}Co like decay up to about day +300. This is followed by a plateau-like phase with an almost constant bolometric luminosity (+300 to +450 d) and, finally, a new decay with a rate close to that of ^{56}Co.

In Section 3, we will argue that most probably in SN 1996al, the CSM/ejecta interaction is the primary energy source for a large part of its evolution. However, comparing the early part of the linear tail of SN 1996al, between ∼150 and 300 d after explosion, with the radioactive tail of SN 1987A, one can derive an upper limit for the ^{56}Ni ejected in the explosion. Assuming a ^{56}Ni mass of 0.075 ± 0.005 M$_\odot$ for SN 1987A (Danziger 1988; Woosley, Hartmann & Pinto 1989), and adopting for SN 1996al a scaling factor of 0.24 as suggested by Fig. 4, we derive that the ^{56}Ni ejected in the explosion of SN 1996al is $\lesssim 0.018 \pm 0.007$ M$_\odot$, where the error budget is equally dominated by the uncertainties on the SN 1996al distance, the epoch of the explosion and the SN 1987A ^{56}Ni mass. We can also estimate the ^{56}Ni mass from the observed luminosity assuming full γ-rays trapping and a rise time to maximum of 10 d. Hence, the amount of ^{56}Co necessary to fit the tail from 100 to 300 d is $\lesssim 0.017 \pm 0.003$ M$_\odot$, fully consistent with that derived from the SN 1987A scaling.

A summary of the main parameter values inferred for SN 1996al and its host galaxy is provided in Table 3.

Table 3. Main parameter values for SN 1996al and its host galaxy.

Parent galaxy	NGC 7689
Galaxy type	SABc[a]
Recession velocity	1970 km s^{-1}[a]
Distance modulus (H_0 = 73 km s^{-1}Mpc^{-1})	31.80 ± 0.2 mag
$E(B-V)$	0.11 ± 0.05 mag
RA$_{SN}$ (J2000.0)	$23^h33^m16^s.29 \pm 0.03$
Dec.$_{SN}$ (J2000.0)	$-54°04'59''.69 \pm 0.05$
Offset from galaxy nucleus	30 arcsec N
Date of B, V maxima (MJD)	50265 ± 2.0 (1996 June 30)
Magnitude at max	$B = 13.7 \pm 0.3$, $V = 13.9 \pm 0.3$ mag
β^B_{100}	4.84 mag

Note. [a]From NED.

2.4 Spectroscopy

Spectroscopic observations spanned from days +23 to +5542, with an excellent temporal coverage during the first two months. Table A2 lists the date (column 1), the Modified Julian Day (column 2), the phase relative to $t_{V_{max}}$ (column 3), the wavelength range (column 4), the instrument used (column 5) and the resolution as measured from the full width at half-maximum (FWHM) of the night-sky lines (column 6). At some epochs, almost contemporary spectra were obtained. These were merged to produce higher S/N spectra or wider wavelength ranges.

The spectra were reduced following standard MIDAS and IRAF routines. The XShooter (Vernet et al. 2011) spectra were reduced using the ESO-XShooter pipeline version 1.1.0. One-dimensional spectra were extracted weighting the signal by the variance based on the data values and a Poisson/CCD model using the gain and readout-noise parameters. The background to either side of the SN signal was fitted with a low-order polynomial, and then subtracted. The flux calibration and telluric absorptions modelling were achieved using spectra of spectrophotometric standard stars. Most spectra were taken through a slit aligned along the parallactic angle, or normalized to spectra taken with a wider ($\gtrsim$ 5 arcsec) slit. The flux calibration of the spectra was checked against photometry (using the IRAF task STSDAS.HST_CALIB.SYNPHOT.CALPHOT) and, if discrepancies occurred, the spectral fluxes were scaled to match the photometry. On nights with fair sky transparency, the agreement with photometry was within 15 per cent. The spectra of SN 1996al are shown in Fig. 5.

2.4.1 A brief description of the overall spectroscopic evolution

The earliest spectra show a relatively blue continuum (T_{bb} ∼ 12 000 K), once corrected for reddening and redshift. The continuum becomes progressively redder with phase, reaching a temperature of about 6500–7000 K at phases later than ∼60 d (see also

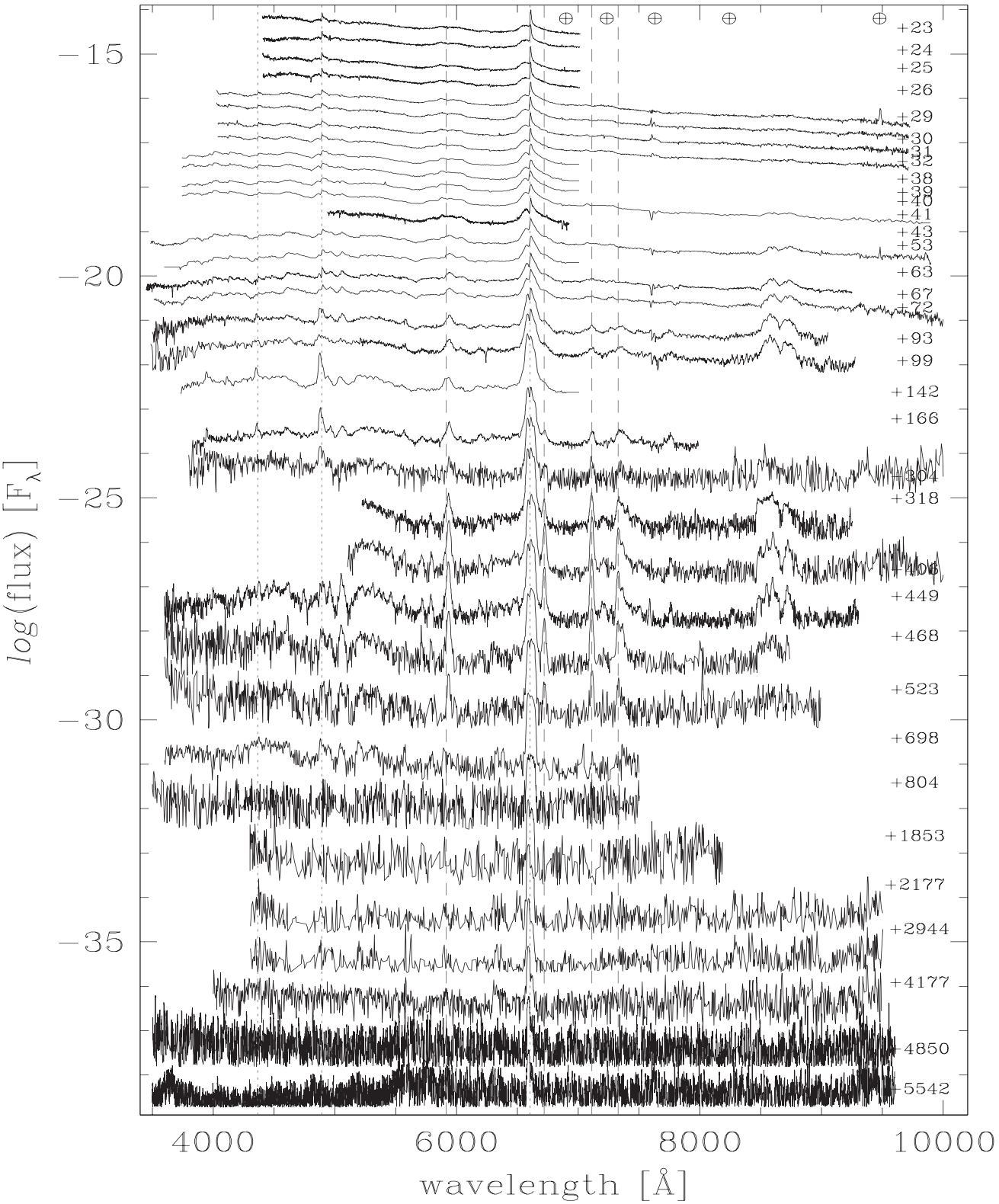

Figure 5. Spectral evolution of SN 1996al. Wavelengths are in the observer's frame. The ordinate flux scale is optimized to the first spectrum, and all others are arbitrarily shifted downwards. In a few cases, noise spikes have been manually removed. From blue to red wavelengths, the dotted (blue) vertical lines mark the positions of H γ, Hβ and Hα, respectively; while the dashed (red) lines mark the 5876, 6678, 7065 and 7281-Å He I transitions. The positions of the most intense telluric absorption bands are marked.

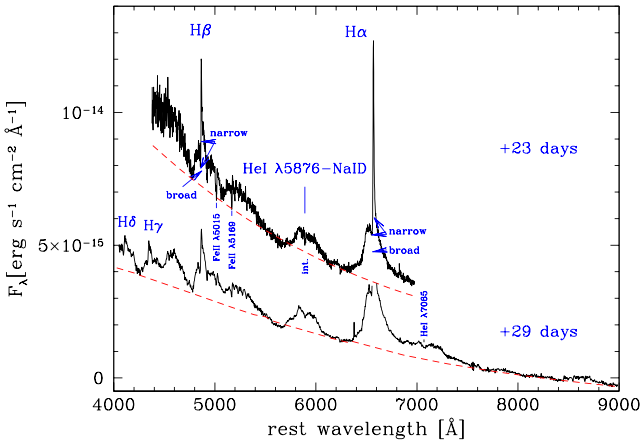

Figure 6. Earliest spectra of SN 1996al corrected for redshift and reddening. The main features are identified, together with the different components seen in Hβ and Hα. The narrow absorption (marked 'int.') on the top of the He I λ5876–Na ID emission is due to Na ID Galactic absorption. The dashed (red) lines are blackbody fits of the spectral continuum (T = 10 100 and 8600 K for +23 and +29 d, respectively; see Section 3.4).

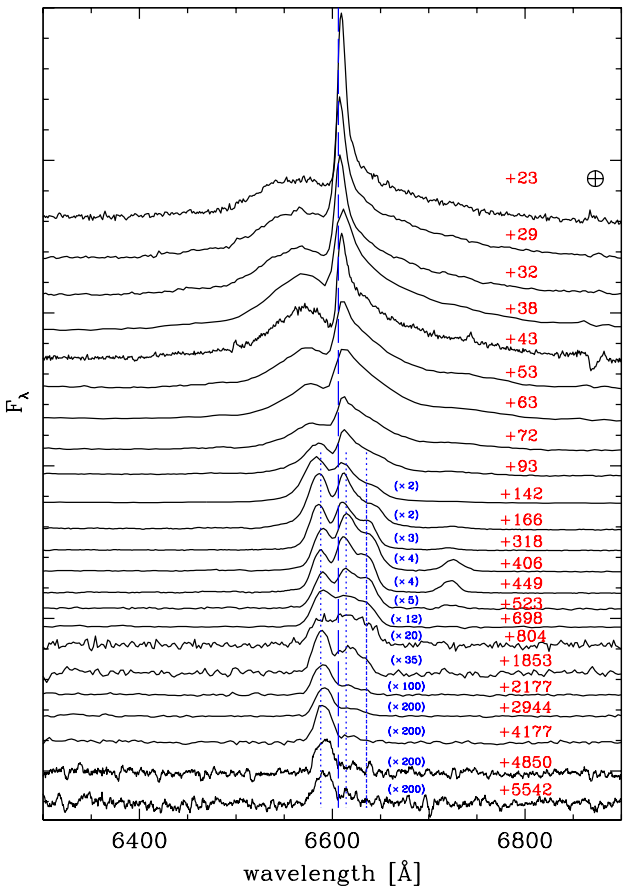

Figure 7. Hα profile evolution of SN 1996al. Wavelengths are in the observer's frame. The feature near 6875 Å in the +43 d spectrum is a residual from an poorly removed telluric band.

Section 3.4). Early spectra are dominated by broad Hα and Hβ, and the blend of He I 5876 Å–Na ID lines.

The Balmer lines show complex profiles (see Figs 6 and 7), and the decomposition of the early Hα profile is detailed in Fig. 8(a).

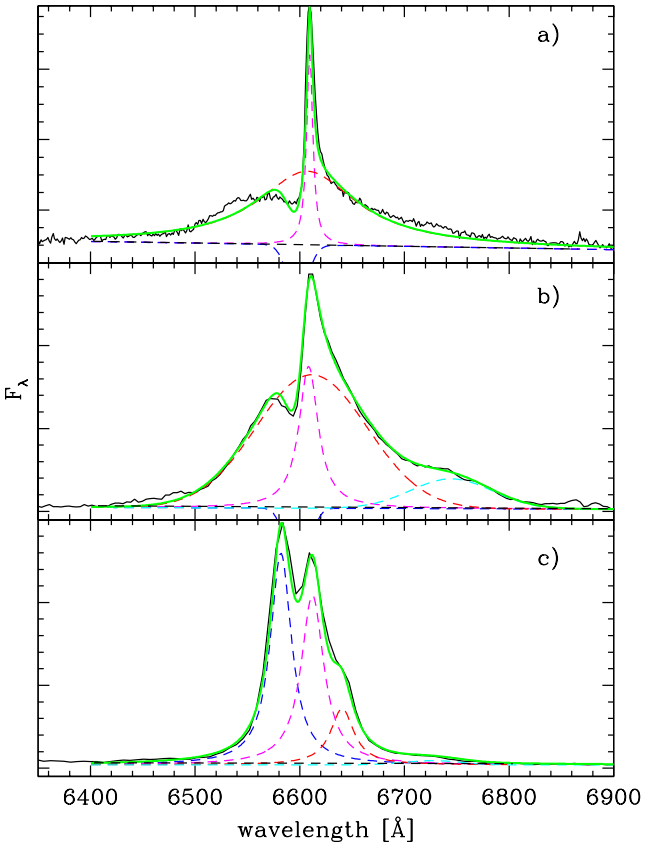

Figure 8. Deconvolution of the Hα profile of SN 1996al at phases +23 d (a); +53 d (b) and +142 d (c), key epochs which attest the profound modification of the line profile. Wavelengths are in the observer's frame. In panels (a) and (b) the Hα line profile has been fitted with a broad emission (Lorentzian in the first, Gaussian in the second; dashed red line), a narrow Lorentzian emission component (dashed magenta line) and a narrow Gaussian absorption component (dashed blue line; cut down for display purpose). The feature redwards of Hα in the +53 d spectrum (Gaussian; dashed cyan line) is He I 6678 Å. In panel (c) the Hα profile has been fitted with three Lorentzians: the Blue (dashed blue line), the Core (dashed magenta line) and the Red component, respectively. The He I 6678 Å line (Gaussian; dashed cyan line) is also present, although now much fainter (see Section 3.3).

Hβ has a very similar profile. The detailed evolution of the Balmer lines (in particular Hα) is discussed in Section 3.2.

Another intense broad emission detected in our first spectrum is a blend of the He I 5876 Å–Na ID lines. It has an FWHM of ∼260 Å centred at ∼5906 Å, though it shows a double-peaked profile (see Fig. 6). The detailed evolution of this and other unblended He lines will be discussed in Section 3.3.

A broad absorption is observed with a minimum at 5079 Å. Assuming it is Fe II 5169 Å, it gives an expansion velocity of ∼5200 km s^{-1}. Also, our early spectra show narrow Fe II (5018–5169 Å) lines with P-Cygni profiles. These are clearly visible in the SN spectra up to phase +43 d, with a mean velocity from the absorption minima of 480 ± 150 km s^{-1}.

The narrow lines likely arise from a dense CSM, which was ionized either by the X-UV flash shock break-out, or by the UV photons emitted by the progenitor star (as suggested by the Hα emission seen around the progenitor before the explosion, cf. Section 3.1). The CSM, which is recombining at these phases, has a bulk velocity of ∼250 km s^{-1}, as deduced from Hβ narrow

emission, but extends up to ∼2000 km s^{-1}, as inferred from the blue edge of the narrow Balmer absorptions.

The spectrum does not change significantly during the first few weeks, with the continuum becoming progressively redder. At phase +29 d, we are able to monitor for the first time a more extended wavelength range (see Fig. 6). Starting from the blue-end of the spectrum, we see H δ and H γ. They have complex profiles similar to those of Hβ and Hα. Redwards to Hα, there is possible evidence for the He I 7065 Å transition (see discussion in Section 3.3), while the He I 6678 Å might be embedded in the Hα red wing.

The +41 d spectrum shows broad emissions (centred at 8531 and 8677 Å) due to the Ca II IR triplet. The FWHM of the total emission is about 3500 km s^{-1}. The He I 5876 Å–Na ID feature still has a very broad profile similar to the emission redwards of Hα, which we interpret as mostly due to He I 7065 Å.

The subsequent spectrum (phase +53 d) shows the appearance of other important features. The broad Hα profile is now better reproduced with a Gaussian profile (having an FWHM∼5700 km s^{-1}, see Table A3), and its red wing is better fitted adding a broad (FWHM∼4500 km s^{-1}) emission centred at 6699 Å (rest frame) in Fig. 8(b). We identify this emission as the He I 6678 Å transition.

In general, the He I lines become more symmetric and narrow with time, with their flux sharply rising after +300 d (cf. Section 3.3). The He I transitions show peculiar line ratios (see Fig. 5 and Tables A3, A4) and then disappear at about phase +700 d (see Section 3.3 for a detailed discussion on the He I lines evolution).

As at these early epochs the FWHM velocities of the Hα broad component are similar to those of the He I lines, it is plausible that these lines originate in the same region of the ejecta and are probably powered by the same mechanism.

The evolution of the Hα/Hβ ratio tells that this mechanism is not photoionization. In fact, starting from phase +43 d this ratio starts a linear increase from a value close to the case B recombination value of 2.8, to ∼10–12 about 1000 d after the *V*-band maximum (see Section 3.2).

At epochs ≥+142 d, the Balmer lines undergo another profound change in their profiles (see Fig. 8c). The narrow lines arising in the unshocked CSM are not visible anymore. This could either imply that the ejecta have overtaken the bulk of the denser CSM or, more likely, that the CSM has by that time completely recombined. The Hα profile is now well fitted with three Lorentzians of comparable FWHM centred at 6539, 6569and 6597 Å (see Table A4 and Section 3.2). These components will be visible along the residual SN lifetime. We will refer to them as Blue, Core and Red components. With time, the Core and Red components become weaker and weaker in comparison with the Blue one (see Fig. 7).

As already stressed, Hβ becomes weaker with time with respect to Hα (see Section 3.2), and the Hα/Hβ ratio reaches values exceeding about 15 at the latest epochs.

3 DISCUSSION

3.1 The progenitor star

A search for archival material concerning the parent galaxy of SN 1996al returned a deep Hα image performed for a portion of NGC 7689 with the Rutgers Imaging Fabry–Perot instrument + CCD Camera attached at the Cassegrain focus of the CTIO 4-m Blanco telescope. The image was taken in the context of a work aimed at studying the star formation in the disc of a sample of Sa galaxies (Caldwell et al. 1991). Luckily enough, the portion of NGC 7689 imaged in 1988 September included the zone where SN 1996al appeared eight years later. Unfortunately, these were the first digital observations performed with modern CCDs and at that time CTIO was not yet equipped with a digital archive (CTIO director, private communication). For this reason, the original frames stored on a 9-track tape by the observer were lost. In order to properly place the SN location on the map we digitalized Plate 29 of Caldwell et al. (1991) and aligned it with the VLT+FORS2 Hα frame obtained under good seeing conditions on 2002 June 16 (see caption of Fig. 1). After the alignment, performed with about 40 sources around the SN positions, we found that a faint Hα region is coincident with the SN position, within an uncertainty of ±0.75 arcsec Given the relatively clean environment at that position (cf. Fig. 1), we believe that the Hα emission visible in the Caldwell et al. (1991) image was indeed associated with the progenitor star of SN 1996al.

The Hα luminosity of this source measured by Caldwell et al. (1991) but not reported in their original paper, given the distance and reddening assumed in this work (see Table 3), is log $L_{H\alpha}$ ∼ 37.28 ± 0.10 dex. For consistency, we checked the Caldwell et al. (1991) Hα measurements of few H II regions close to the SN 1996al position with those derived from the FORS2 Hα frame, and found a very good agreement.

The Hα pre-explosion luminosity is compared with those of some possible progenitor systems for SN 1996al in Table 4. The comparison indicates that the Hα emission coming from the SN 1996al progenitor is similar to that expected from hot Luminous Blue Variables (LBV) stars, and lower than that measured in SN-impostor/LBVs prior to a major outburst. This is consistent with the finding of

Table 4. Main parameter values for SN 1996al progenitor systems.

Name	Spectral type	log $L_{H\alpha}$	Reference
SN 2009ip	SN-impostor/LBV	38.71[a]	1
SN 2000ch	SN-impostor/LBV	38.48[b]	2
UGC2773−2009OT	SN-impostor/LBV	38.38[c]	3
η Car	LVB/O5.5III–O7I	37.55[d]	4
AG Car	LBV/B2/3Ib–WN11	37.54[e]	5
S Dor	LBV/A5Iaeq C	37.04[f]	4
HR Car	LBV/B7Ve C	36.41[g]	4
ζ^1 Sco	LBV/B1Ia–Oek C	35.32[h]	4
SN 1996al prog	–	37.28	This paper

Notes. [a]Average values of three epochs (2010-10-06; 2011-09-02; 2011-09-24); assumed μ = 31.55 mag and $E(B-V)$ = 0.019 mag from Smith et al. (2010). [b]Average of two epochs (2000-05-06; 2009-05-19); assumed μ = 30.17 mag and $E(B-V)$ = 0.013 mag from Pastorello et al. (2010). [c]Average of three epochs (2012-07-20; 2009-09-05; 2010-01-26); assumed μ = 28.95 mag and $E(B-V)$ = 0.5 mag (only Galactic) from NED (http://nedwww.ipac.caltech.edu). [d]Measurements from the 2009-04-16 epoch; assumed distance of 2.3 kpc from Walborn (2012) and $E(B-V)$ = 0.55 mag from Humphreys & Martin (2012); spectral type from SIMBAD (http://simbad.u-strasbg.fr/simbad/). [e]Average over eight years of measurements; assumed distance of 6 kpc from Humphreys et al. (1989), Hoekzema, Lamers & van Genderen (1992) and $E(B-V)$ = 0.65 mag from Shore, Altner & Waxin (1996); spectral type from SIMBAD. [f]Average of four epochs (2008-02-04; 2009-02-08; 2009-09-15; 2010-08-03); assumed distance go 49.97 kpc from Pietrzyński et al. (2013) for LMC and $E(B-V)$ = 0.12 mag from Massey (2000); spectral type from SIMBAD. [g]Average of two epochs (2008-12-13 and 2010-04-01); assumed distance of 5 kpc and $E(B-V)$ = 0.9 mag from van Genderen et al. (1991); spectral type from SIMBAD. [h]Average of two epochs (2009-10-19; 2010-07-04); assumed distance of 2 kpc and $E(B-V)$ = 0.66 mag from Crowther, Lennon & Walborn (2006); spectral type from SIMBAD. 1 = Pastorello et al. (2013). 2 = Pastorello et al. (2010). 3 = Pastorello et al., in preparation. 4 = Richardson et al. (2012); Richardson, private communication. 5 = Stahl et al. (2001).

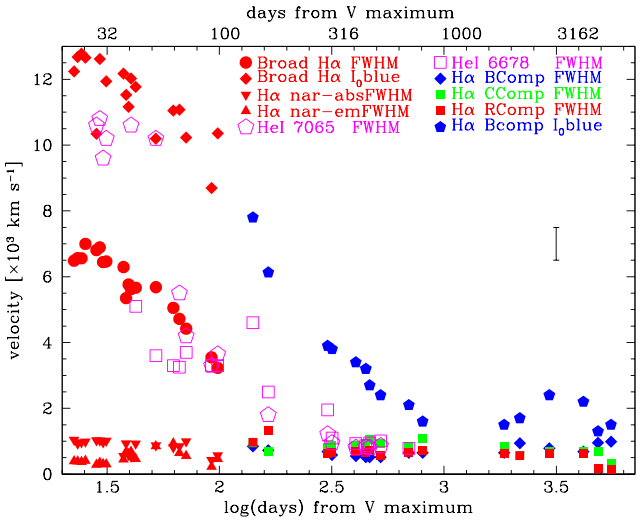

Figure 9. Velocity evolution of the Hα components and the He I 6678–7065 Å transitions. The mean error bar (±500 km s^{-1}) for the broader lines is shown. For the narrowest features (those with FWHM$\lesssim$ 2000 km s^{-1}), the error bar is smaller than the symbol.

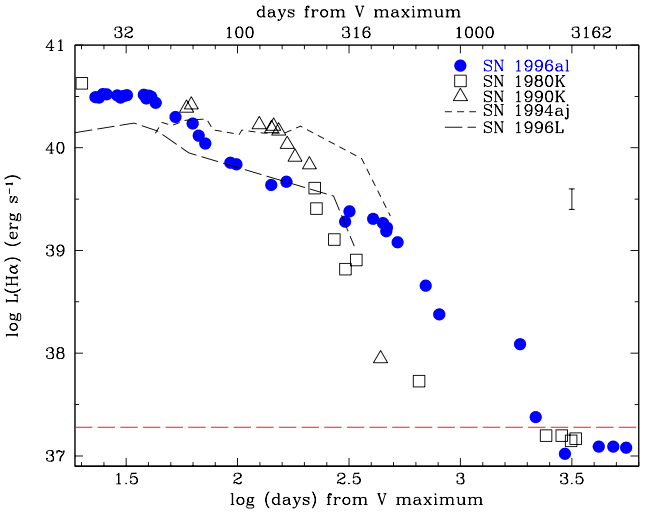

Figure 10. Hα luminosity evolution of SN 1996al compared with those of SNe 1980K (Uomoto & Kirshner 1986), 1990K (Cappellaro et al. 1995), and the twin SNe 1994aj (Paper I) and 1996L (Paper II). The mean error for the log ($L_{H\alpha}$) of ±0.10 dex is reported. The horizontal long-dashed (red) line marks the Hα flux emitted by the precursor star. The Hα luminosities here reported are the total Hα flux measurements, which may be slightly different from the sum of the fitting components reported in Tables A3 and A4 and resulting from the deconvolution of the entire line profile. The Hα luminosity on day +4178 is the average between the flux measured from the FORS2 spectrum and that derived from the calibrated Hα image.

Kennicutt & Hodge (1980), that H II regions in NGC 628 with log $L_{H\alpha}$ < 37.90 dex have a radius <200 pc, and are supported by the radiation field of a star with a spectral type later than O4 Ia.

After profile decomposition (see Fig. 8 and Table A3), the narrow Hα component visible in the first SN spectrum has a flux of ∼9 × 10^{-14} erg s^{-1} cm^{-2}, which provides a line luminosity of log L∼39.85 dex. This is more than 2 dex higher than the pre-explosion Hα luminosity (see Table 4). The abrupt increase of the narrow Hα luminosity is a clear indication that the SN shock break-out or ejecta/CSM interaction ionized a much larger fraction of CSM around the progenitor star than the SN progenitor alone.

3.2 The evolution of the Balmer lines

The profile of Balmer lines, in particular Hα, shows a multicomponent, complex evolution which allows us to track the restless mass-loss activity of the progenitor star. It also indicates an asymmetric distribution of the emitting gas. In the following, we will have a close look into the Hα evolution in four temporal intervals.

Days +23 to +43: the Hα profile consists of a broad Lorentzian emission with, superposed, a narrow P-Cygni like component. The Hα profile does not change (see Fig. 7) until phase $\lesssim$ +40 d, which coincides with the end of the 'short plateau' (see Fig. 2).

At the same time, the expansion velocity obtained from the Hα FWHM of the broad component decreases from ∼6500 to ∼5600 km s^{-1}, while the maximum velocity deduced from the Hα blue wing remains constant at about 12 000 km s^{-1} (see Table A3 and Fig. 9). The average wind velocity as given by the width of the narrow emission shows some scatter around the value of ∼440 km s^{-1}. The mean FWHM of the narrow absorption is about 890 km s^{-1} (see Table A3 and Fig. 9).

The Hα luminosity evolution is negligible (see Fig. 10), and the Hα/Hβ flux ratio, which remains constant at about 2.68 (see Fig. 11), is close to case B recombination (Osterbrock 1989).

Days +53 to +101: the broad Hα is now best fitted by a Gaussian profile with an FWHM decreasing from 5700 to 3250 km s^{-1}, though faint extended wings are still visible (see Fig. 8b). The maximum velocity deduced from the Hα blue wing remains, instead, constant at about 10 500 km s^{-1} (see Table A3 and Fig. 9).

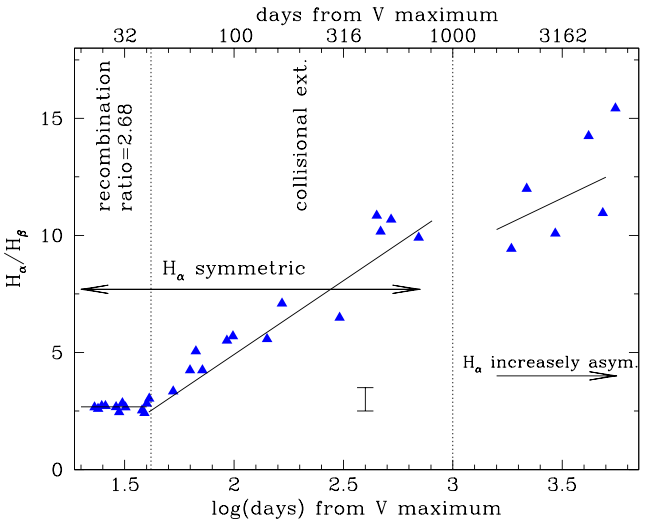

Figure 11. Evolution of the Hα/Hβ ratio for SN 1996al. The changes of the main properties of Hα are labelled. The latest points, after 1000 d, are essentially lower limits since (at these late phases) Hβ barely detectable. The mean error bar for the Hα/Hβ ratio (±0.5) is shown.

Again, these velocities are similar to those of the He I lines, hence we suppose that the lines originate in the same region of the ejecta. Since in the next section we will demonstrate that at these phases the He I lines are powered by ejecta–CSM interaction, we believe that the same mechanism also supports the Hα flux. At day +100, the Hα luminosity is about 0.3 dex lower than the Hα luminosity for the twin SN 1994aj at the same phase (Paper I), but is very similar to that of SN 1996L (Paper II).

The velocity of the wind, as derived from both the narrow emission and absorption features, shows a mean value of ∼590 km s^{-1}.

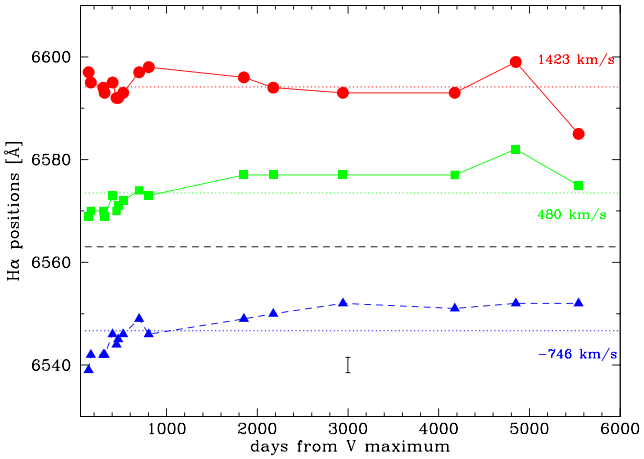

Figure 12. Evolution of the positions of the three Hα components in the spectra of SN 1996al obtained after day ∼100. The mean error bar for the component positions (±1.5 Å) is shown.

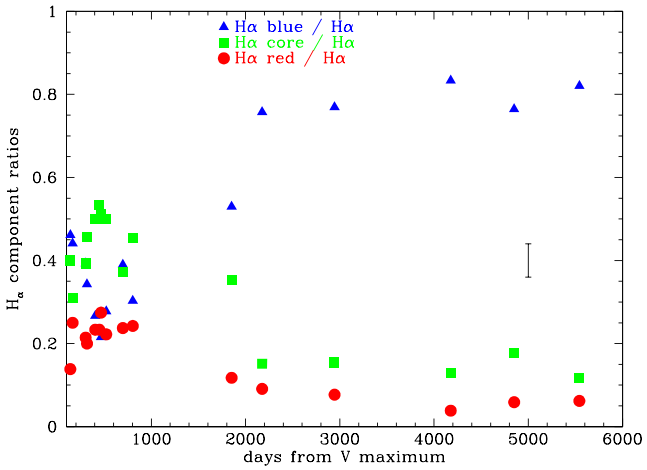

Figure 13. Evolution after day ∼100 of the flux ratios of the three Hα components in the spectra of SN 1996al. The flux of each component is divided by the total flux. The mean error bar for the flux ratios (±0.08) is shown.

In this period, the Hα/Hβ flux ratio begins to increase, reaching a value of ∼6.5 at a phase of +100 d. This could be a clue that Hα becomes more collisionally excited (Branch et al. 1981), in line with the proposed scenario (see Section 3.5).

Days +142 to ∼ +800: from day +142, the Hα profile undergoes another profound change. The Hα profile is now better fitted by three Lorentzian components (see Fig. 8c), up to phase +523 d, and later on with three Gaussian components. They are centred at ∼− 1100 km s^{-1} (the Blue component), 270 km s^{-1} (the Core component) and +1550 km s^{-1} (the Red component) with respect to the nominal position of Hα.

The three narrower components are visible along the remaining life of the SN and their wavelengths do not change significantly with time (see Figs 7 and 12).

Since their earliest appearance, these components show a very similar FWHM, the Red component being the broadest (FWHM∼970 km s^{-1}), followed by the Core component (FWHM∼950 km s^{-1}), while the Blue component has an FWHM∼850 km s^{-1}(see Table A4 and Fig. 9).

Between 142 and 800 d, the flux ratios of the different components stay constant, with the Core and Blue components carrying the largest fraction of the Hα flux (30–40 per cent each). In this lapse of time, the Hα luminosity shows a relatively flat and linear (in a log–log diagram) decrease up to phase ∼+ 500 d, followed by a sharper drop (by almost 1 dex) up to about +800 d. This behaviour resembles that of the bolometric curve which, however, stops at about 700 d after explosion (see Fig. 4).

We interpret these Hα components as the result of the interaction between a mostly spherical ejecta with an highly asymmetric CSM. The geometric configuration of the system will be discussed with more detail in Section 3.5.

The Hα/Hβ flux ratio continues to steadily rise (see Fig. 11) to a value of about 10.

Later than +800 d: there is an observational gap between +800 and +1850 d. From day +1853 the Hα profile is again fitted by the three Gaussians mentioned before, and both the Hα flux and the bolometric curve show steeper evolutions.

While the overall flux carried out by the line dim by 0.28 dex during this time interval, the relative intensities of the three components change: the Blue component is now much stronger with respect to the other two, while the Red one remains the dimmest (see Fig. 13).

At phase +2177 d, the flux ratio of the Core component decreases to the level of the Red component one, while the Blue component is carrying almost 80 per cent of the line flux. After this phase, the line ratios do not change very much. The sharp change in the relative flux ratios may be a signature of either a sudden dust formation in the SN ejecta, or a progressive quenching of the interaction between the ejecta and the receding part of the CSM. Most probably, as the central wavelengths of the Core and Red emission peaks do not show any evolution (see Fig. 12), both scenarios are at work. Also the Blue component does not show any shift from the central position. For this reason, if dust is forming, it condensates in the inner part of the ejecta or in the clumps where the Core and Red Hα components originate.

Starting from ∼2900 d after the explosion, the Hα luminosity (see Fig. 10) decreases below the luminosity emitted by the precursor star. This, along with its distorted profile, proves that most of the Hα flux comes from the SN itself and that the ambient contamination is by now negligible. Moreover, this is a clue that the Hα source detected before the explosion was indeed associated with the precursor star and that it has been swept up by the SN ejecta.

3.3 The He I lines

In our first spectra, the best evidence for the presence of helium is the broad asymmetric bump (FWHM∼11 000 km s^{-1}) centred at about 7065 Å (rest frame) that can be identified as He I 7065 Å (see Fig. 6). Figs 14 and 15 show the complete evolution of He I 7065 Å, the only helium transition which is not contaminated by close-by strong lines. In fact, this is not the case for He I 5876 Å, which could be heavily contaminated by the nearby Na ID doublet. An estimate of the relative contribution of two lines throughout the complete spectroscopic evolution of SN 1996al is a very difficult task. The last phase in which the He I lines are unequivocally detected is +523 d (see Fig. 5).

In Fig. 16, we compare the profiles of He I 5876 Å–Na ID with the He I 7065 Å line, during the first 100 d of the SN evolution. In the first two spectra (+29 and +32 d) they are very similar, both in the overall profile and velocity limits. The lines show a double peaked profile with the blue one peaking at ∼− 2000 km s^{-1}and the red one at ∼3500 km s^{-1}, with the red wing extending far to

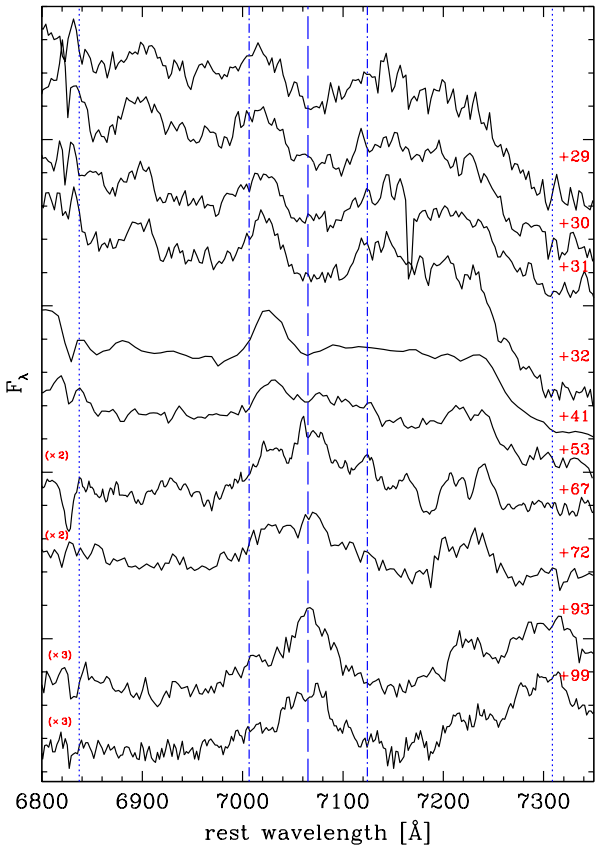

Figure 14. Evolution of the He I 7065-Å line profile during the first 100 d. The dashed line marks the He I 7065-Å rest-frame position, while the dotted and dash–dotted lines show the expansion velocities of ±10 000 and ±2500 km s^{-1}, respectively.

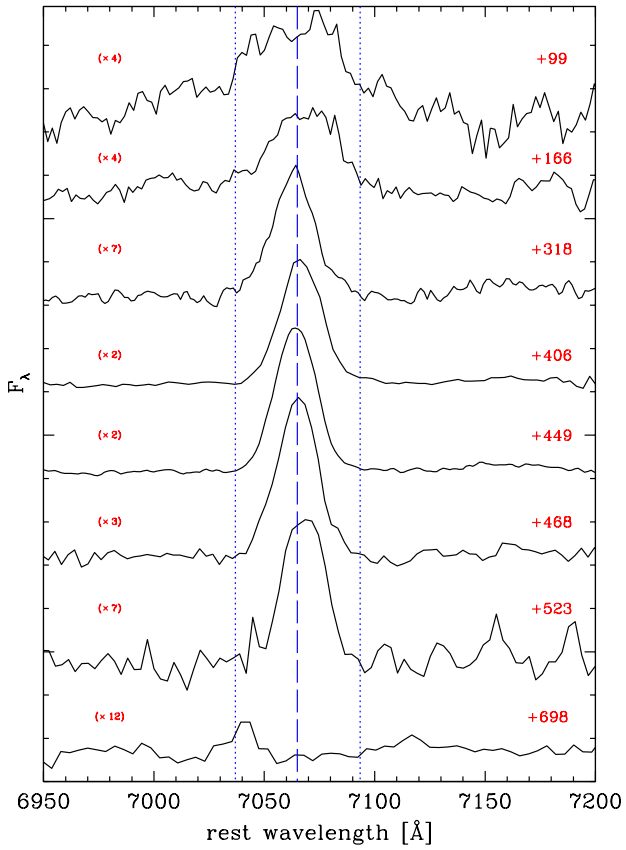

Figure 15. Evolution of the He I 7065-Å line profile after 100 d. The dashed line marks the He I 7065-Å rest-frame position, while the dotted lines indicate the expansion velocity of ±1200 km s^{-1}.

higher velocities (∼9000 km s^{-1}) than the blue one. Thanks to the similarity of the profiles, we may safely conclude that at phases +29, and +32 d the He I 5876 Å–Na ID feature is almost entirely due to He. Fig. 16 shows that, at least during the first month, the broad wings of the Hα profiles are similar to those of He I lines, suggesting that the three lines form in the same, asymmetric region.

Fig. 14 also shows that the profile of the He I 7065 Å emission remains unchanged up to +53 d after the *V* maximum, with the blue bump dominating the line profile. By this time, the profile of He I 5876 Å–Na ID feature starts to deviate from that of He I 7065 Å (see Fig. 16) with a broad bump emerging slightly redder than the Na ID rest wavelength position. Apart from this difference, the two He I lines and the broad Hα still share the same basic characteristics (see third panel from top in Fig. 16).

Starting from phase +67 d, the He I 7065 Å line shows a new component centred at the rest position, with the blue and red bumps still being visible. Also the He I 5876 Å–Na ID feature has an overall similar profile, with an increasing contribution from the Na ID.

Afterwards, (on day +93 and +99) the He I 7065 and 7281 Å features become progressively more symmetric, are centred at the rest position and reach terminal velocities of about 2500–3000 km s^{-1} (see bottom spectra in Fig. 14). The He I 5876 Å–Na ID profile is different, indicating an increased contribution by Na ID (see below). On the contrary, the terminal velocities of the Hα broad component are higher, implying different zones of formation. The broad Hα component is still coming from the outer fast-moving region of the ejecta whose emissivity strongly depends on CSM interaction, while the He–Na ID lines mostly form in the slow expanding spherically symmetric inner ejecta.

In order to explain the broad He I line profiles at early times, we may conceive two possible alternatives: either some ^{56}Ni was ejected at high velocity (∼10 000 km s^{-1}), or the He I lines were supported by the interaction of the fast expanding symmetric ejecta with an asymmetric CSM. Since starting from about two months past explosion the He I lines become symmetric (the inner geometry of the innermost layers appears to be symmetric), we believe that the interaction scenario is the most likely.

The disappearance of the He I 5876 Å emission line after about day +100 is prima facie at odds with the presence of the pronounced He I 7065 Å emission. The clue can be found in the coeval emergence of the Na ID emission. In fact, in a comoving frame the He I 5876 Å photon emitted by the SN ejecta can be redshifted and scattered into the Na ID. As a result we see the Na ID feature instead of the He I 5876 Å emission. The mechanism can be explored through a model based on a Monte Carlo simulation (Fig. 17). The underlying model assumes freely expanding spherical ejecta with the He I 5876 Å emissivity distribution recovered from the He I 7065 Å profile (Fig. 17, inset). The adopted He I 5876 Å flux is 1.2 times larger than that of He I 7065 Å, corresponding to the case of collisional excitation dominating over recombination (Almog & Netzer 1989). The optical depth of the Na ID is assumed to linearly fall with increasing velocity from $\tau(5890) = 20$ at the SN centre ($v = 0$), to zero at $v = 1800$ km s^{-1}. The relative fractions of the Rayleigh and spherical scattering are determined by the Hamilton parameter E_1 which, in the representation of Chandrasekhar (1960), is 1/2 for Na I

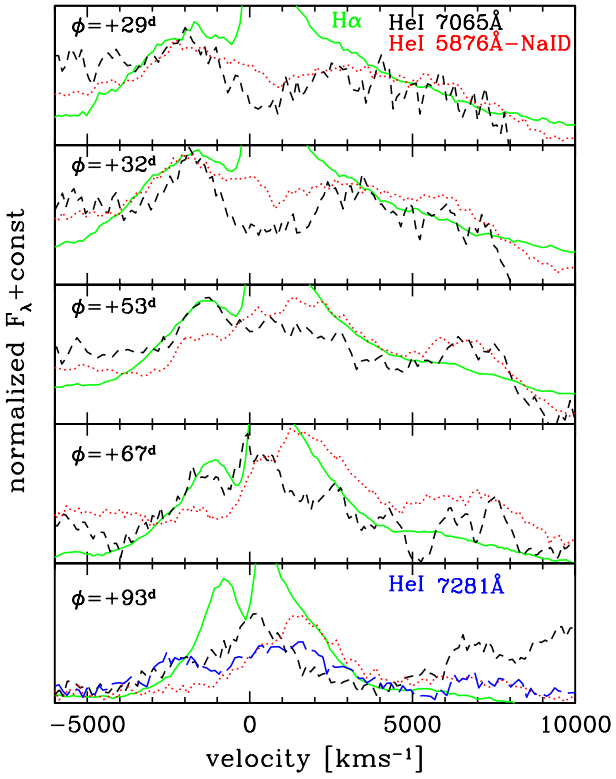

Figure 16. Comparison in the velocity space of the profile evolution of the He I 5876 Å–Na ID feature (reference wavelength is 5876 Å, dotted red lines) with those of the He I 7065 Å feature (short-dashed, black lines) and Hα solid green lines. In the last phase (+93 d), we also show the profile of He I 7281 Å feature (long-dashed blue line).

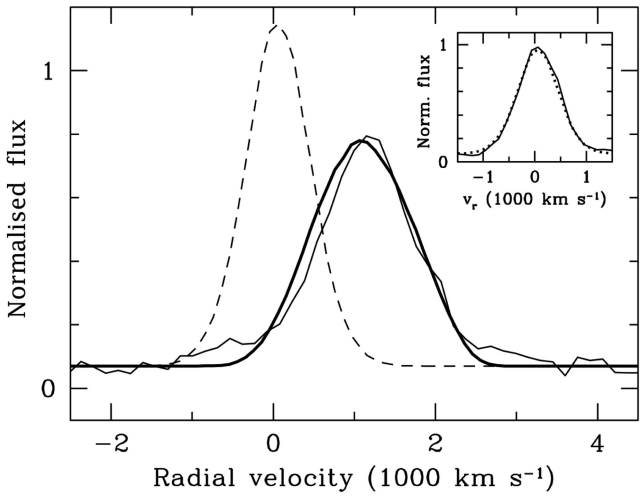

Figure 17. Effect of the non-local scattering of the He I 5876 Å emission by the Na ID in SN 1996al. The observed spectrum on day +406 (thin solid line) is compared with the model spectrum (thick solid line). The latter is the result of the scattering of the mock-up He I 5876 Å emission (dashed line) in the optically thick Na ID lines. The scaled mock-up He I 5876 Å profile (dotted line) is compared with the observed He I 7065 Å line in the inset. The radial velocity scale refers to the He I 5876 Å line.

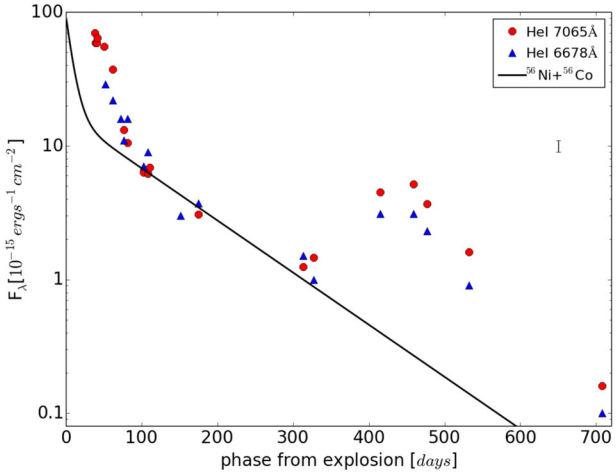

Figure 18. Flux evolution of the He I 6678 and 7065 Å lines. The fluxes have been reddening corrected. The ^{56}Ni+^{56}Co fitting law is similar to that used for fitting the bolometric light curve of Fig. 4 and has been tuned to fit the +100to + 300-d flux points. As in Fig. 4, a rise time to maximum of 10 d has been assumed. A mean error bar for the line fluxes is reported.

5890 Å and zero for Na I 5896 Å. In the optically thin limit, therefore, the scattering phase function for Na I 5896 Å line is spherical, while for Na I 5890 Å line the phase function is the superposition of the spherical (1/3) and Rayleigh scattering (2/3). The latter is taken into account for optical depth $\tau(5890) \leq 1$. For $\tau(5890) > 1$, the scattering is assumed to be spherical. This approximately accounts for the scattering spherization during the multiple local scattering. It is reassuring that the simulated spectrum (Fig. 17) from this simple model provides an excellent fit to the observed emission line.

The evidence of the non-local scattering of He I 5876 Å photons into Na ID implies that the late time He I line originates in the inner layers of the SN ejecta.

Fig. 15 shows the evolution of the He 7065 Å emission up to almost two years after explosion. While the flux evolution of the line shows a bump between +300 and +500 d (see Table A4 and Fig. 18), it becomes narrower with a terminal velocity of about 1200 km s^{-1} (see Fig. 9).

The flux evolution of the He I 6678 and 7065 Å lines reported in Fig. 18 shows that the evolution of the line fluxes is consistent with that of the ^{56}Co decay in the time interval +100 to + 300 d, while at earlier and later phases some extra energy from the interaction between the ejecta and CSM is required.

Despite the fact that the CSM/ejecta interaction is likely the primary source for the SN luminosity, the mechanism responsible for the evolution of the He I emission is far from being clear. On day +449, the He I 7065 Å luminosity is $\sim 4 \times 10^{38}$ erg s^{-1}. The He I 5876 Å and He I 10 830 Å lines are typically stronger than the He I 7065 Å line by 1.2 and 4–5 times, respectively (Almog & Netzer 1989). The total He I luminosity around day +450 is estimated to be $\sim 2.8 \times 10^{39}$ erg s^{-1}, which is larger than the total Hα luminosity of 2×10^{39} erg s^{-1} and significantly larger than the luminosity of the Hα Core component. This fact and the low velocity of He-emitting gas suggest, again, that the helium emission originates from the He-rich central zone of the SN ejecta.

Interestingly, the Hα line does not show a significant luminosity enhancement during +300to + 450 d (see Fig. 10), when the He I 7065 Å flux increases by a factor of 4. This may be understood if the hydrogen ionization fraction is close to unity, so that the hydrogen emission does not react to the enhanced ionization that leads to the

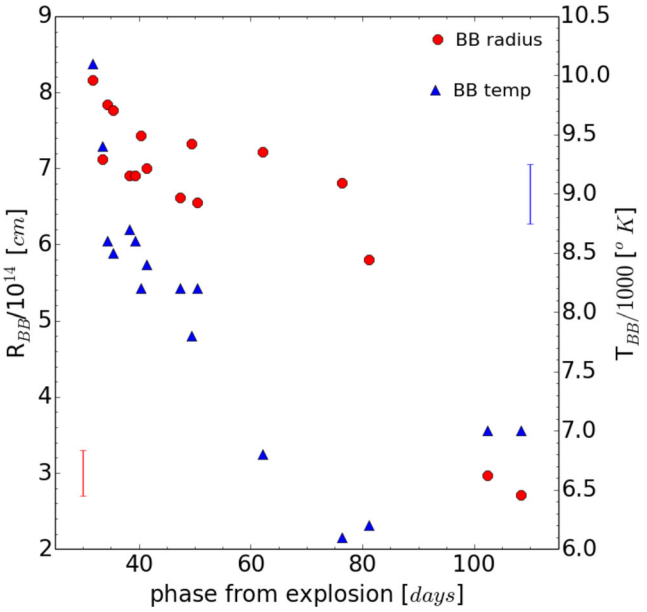

Figure 19. Evolution of the blackbody radius and the temperature in days from the explosion, assumed to occur 10 d before the maximum light. The average temperature error bar of ±250 K is shown in the upper-right corner, while the mean error bar for radius (±0.3 × 10^{14} cm) is shown in the lower-left corner.

emergence of strong helium lines. If this is the case, then the total mass of hydrogen in the SN ejecta should be close to the mass of the ionized hydrogen, i.e. of the order of 0.1–0.3 $M_\odot$ (see Section 3.5.1). Alternatively, if the helium is ionized by the central source, the X-UV radiation could be strongly attenuated already in the He layer, so that the external hydrogen layer would be only marginally affected.

Two possible sources for powering the transient He I emission are conceivable: X-ray emission from the enhanced CSM interaction or energy release due to accretion into the black hole. The latter requires the accretion of ∼10^{-7} $M_\odot$ during about +200 d and a super-Eddington X-UV luminosity. This could originate in the thermalization of the accretion disc wind in a scenario of disc outflow interacting with the SN ejecta (Dexter & Kasen 2013).

3.4 Photospheric radius

In order to derive the evolution of the photospheric radius and temperature, we perform a blackbody fit to our early time spectra, after correcting for reddening and redshift values reported in Table 3. The fits were done selecting the portions of the spectra free of evident lines (examples of the fits are reported in Fig. 6). The fit errors, which depend on a number of parameters, mainly the wavelength extension of the spectra, lines contamination, the uncertainty of the flux calibration and the assumed extinction, have been estimated to be of the order of 250 K. Adopting the bolometric curve of Fig. 4, spherical symmetry and a filling factor of 1, we estimate the evolution of the blackbody radius and the temperature (Fig. 19). The computation is extended up to 100 d post explosion. This does not imply that the SN has a clear spherical symmetric photosphere up to that epoch (cf. next section).

The photosphere several days after the explosion is relatively hot, with a T_{BB} ∼ 10 000 K and a radius close to 7.4 × 10^{14} cm. While the temperature shows a smooth decrease to about 6500K at a phase of +100 d after explosion, the photospheric radius remains almost at a constant value of about 6.9 × 10^{14} cm up to 80 d after explosion, with a sudden decline to 3.0 × 10^{14} cm at phase about +100to + 110 d (see Fig. 19).

3.5 Parameters of the progenitor star and environment geometry

In the following, we will sketch a scenario for the SN explosion and its environment that will attempt to account for all available observations.

Despite a high expansion velocity of the ejecta (∼10^4 km s^{-1}, see Table A3) as indicated by the broad wing of Hα and the boxy He I 5876 Å emission, the spectra have never shown pronounced broad absorption lines of either hydrogen or other species. This implies that the photosphere is located in the external layer of the SN ejecta. The absence of pronounced broad absorptions is typical of SNeIIn, in which the SN ejecta interact with a dense circumstellar matter (CSM), and is attributed to the high optical depth in the cool dense shell (CDS), that is located at the ejecta/CSM interface (Chugai 2001). It should be emphasized that – in the case of SN 1996al – the CDS is probably patchy because we can detect the broad Hα emission arising in the inner SN ejecta.

The higher resolution spectrum on day +43 (see Fig. 7) showing the pronounced broad and narrow Hα components can be used to probe both the SN ejecta and the CSM. The broad component is emitted by the freely expanding ejecta with maximum velocity of $\lesssim$ 10 000 km s^{-1}, while the narrow line with P-Cygni profile presumably forms in the CSM, which expands with $v < 2000$ km s^{-1}.

With these numbers, it is easy to calculate the radius of the CDS during the first 1–2 months after the explosion (assuming it occurred 10 d before the maximum light), which spans between 3–4 × 10^{15} cm. Given the radii calculated in the previous section, and supposing that the photosphere is placed close to the CDS, an upper limit of ∼10 per cent for the filling factor of the patchy CDS is derived.

3.5.1 Modelling the early Hα profile

The broad Hα line is modelled with the Monte Carlo technique adopting the recombination emission in the ionized ejecta, with the H^+ and n_e distributions described by a broken power law ($n_e \propto v^k$) with power index $k = k_1$ in the inner zone ($v < v_0$) and $k = k_2$ in the outer zone. The Thomson scattering with thermal broadening in the ejecta is taken into account, assuming a kinetic temperature of 10^4 K. Note that Thomson scattering turns out to be a crucial diagnostic probe for estimating the total amount of ionized hydrogen. Since our model does not compute the hydrogen level population, we consider two extreme cases for the Hα optical depth: optically thin Hα line ($\tau_{23} \ll 1$) and optically thick one ($\tau_{23} \gg 1$). The optically thin case is plausible, because the flux in the Balmer continuum seems to be large enough to strongly depopulate the second level. Two sources of continuum are included: the SN ejecta with the emissivity $\epsilon \propto n_e^2$, and the CDS at $v = 10\,000$ km s^{-1}. We do not compute the absolute flux neither in the line nor in the continuum. We neglect the contribution of the line emission from the CDS compared to the continuum radiation bearing in mind that, in the case of the opaque CDS, the contrast of the CDS line emission with respect to the CDS continuum is small. This is indicated by observations of interacting SNe (e.g. SN 1998S at the age of 10–40 d; cf. Fassia et al. 2001) and supported by arguments based on the model of a thin opaque shell with the estimated line-to-continuum contrast of

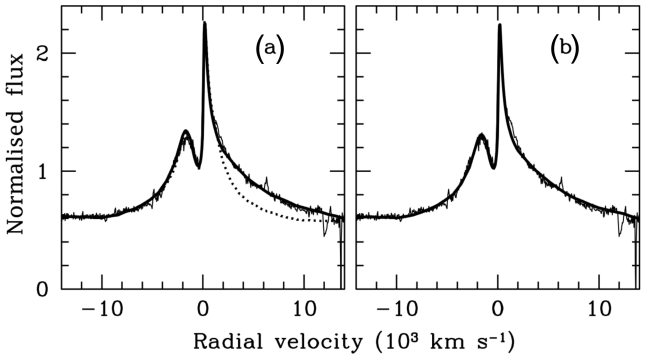

Figure 20. Comparison of the Hα line model with the observed spectrum on day +43 (thin solid line). Panel (a): the SN ejecta with optically thin Hα line (thick solid line) and the same model without Thomson scattering (dotted line). Panel (b): model with optically thick Hα line. In both cases the narrow component forms in the CSM and is primarily due to resonance scattering.

the order of the thermal-to-expansion velocity ratio (Chugai 2001). Instead, we let line and continuum emissivities of SN ejecta to fit the observations. The contribution of the CDS in the line emission is then neglected whereas the continuum radiation of the CDS is taken into account. The angular dependence of the CDS continuum brightness (I_c) affects the strength of the Hα broad absorption. We assume $I_c \propto 1/\cos\theta$, where θ is the angle with the normal to the CDS surface. This approximation holds when the CDS is either optically thin or fragmented in such a way that the average number of clouds on the LOS is less than unity. Strong fragmentation is expected given the fact that CDS is Rayleigh–Taylor unstable (Chevalier 1982). The contribution of the CDS continuum is a free parameter derived from the best fit of the Hα profile. The latter is determined by the normalized distribution of ionized hydrogen along the radius and by the Thomson optical depth.

We show two cases for the broad component: $\tau_{23} \ll 1$ (no Hα resonance scattering) and $\tau_{23} \gg 1$ (Fig. 20). A reasonable fit of the broad component to the observed Hα profile on day +43 is found for the parameters: $k_1 = 1$, $k_2 = -1.7$, $v_0 = 1800$ km s^{-1}, and Thomson optical depth $\tau_T = 2.1$. The case without Thomson scattering (dotted line in Fig. 20a) demonstrates the crucial role of electron scattering for the formation of the line profile. In the case of the optically thick Hα line, we find that the relative contribution of the ejecta continuum is $\leq$10 per cent; for a larger contribution of the ejecta continuum, the broad Hα absorption component becomes prominent. For the optically thin Hα, the calculated recombination continuum in the Case B, can contribute only to 3.3 per cent of the observed continuum. The recovered Thomson optical depth, together with the estimated CDS radius on day +43 and the normalized electron distribution recovered from the Hα profile, suggest a mass of ionized hydrogen of 0.07 M$_\odot$ in the ejecta and an Hα luminosity of 2×10^{40} erg s^{-1} on day +43. The latter is in excellent agreement with the observational estimate.

We now turn to the narrow line. The peak of the narrow emission on days +23 and +43 suggests the presence of the Hα-emitting CS gas with velocities of $\sim$300 km s^{-1}. On the other hand, the wings of the narrow emission profile and the blue edge of the narrow absorption indicate CSM velocities as high as $\sim$2000 km s^{-1}. This is consistent with the expansion law $v \propto r$ for the CSM with a maximum velocity of $\sim$2000 km s^{-1} which is used for the Hα modelling. We adopt the external radius for the fast CSM outflow of 5×10^{15} cm on day +43, keeping in mind that the spectra suggest that this kinematics is maintained at least until day +63. We find that the resonance scattering is a good approximation for the narrow P-Cygni line, although we need to add a net emission which amounts to 8 per cent of the resonant scattering component. We checked also a model where the CSM outflow has a constant velocity. However, such a model reproduced neither the absorption nor the emission components of the narrow line. In the best-fitting case shown in Fig. 20, the Hα optical depth in the CSM decreases outwards from 0.9 at the CDS radius (R_s) down to zero at the boundary radius R_b according to $\tau = 0.9[(r - R_s)/(R_b - R_s)]^{1.6}$.

The kinematics $v \propto r$ followed by the observed narrow Hα poses a question about its origin. Generally, this sort of the kinematics combined with large value of the terminal velocity ($\sim$2000 km s^{-1}) suggests a mass ejection via shock wave. At present, we are not able to propose a reliable mechanism for this vigorous mass-loss. Beside the stellar shock, the common envelope phase in a binary system could also play a role.

3.5.2 *Modelling the light curve*

The fast initial ($t < +100$ d) drop of the bolometric light curve (see Fig. 4) strongly indicates that the diffusion time in the SN envelope is small, which implies low-mass ($\sim$1 M$_\odot$) ejecta. At first glance, this is at odds with the high mass of the SN progenitor suggested by the pre-explosion Hα luminosity ($\sim 10^{37}$ erg s^{-1}, see Table 4). In fact, in the case B recombination, the pre-explosion Hα requires a rate of ionizing radiation of $\sim 10^{49}$ photons s^{-1}. To sustain this ionization rate, we need a hot progenitor star with bolometric luminosity $\log L/L_\odot \gtrsim 5.4$ and radius $R \sim 10\,R_\odot$ (see discussion in Section 3.1). According to atmosphere models (Simón-Díaz & Stasińska 2008), the above precursor may have been a 25-M$_\odot$ Zero age main sequence (ZAMS) star at the final evolutionary stage (Woosley, Heger & Weaver 2002). The apparent controversy between the SN light curve and pre-SN Hα constraints can be solved if one assumes that the 25-M$_\odot$ ZAMS progenitor had lost almost the whole hydrogen envelope, with most of the helium core falling back on to the collapsing core making a black hole (see models in the 25–30-M$_\odot$ mass range of Heger et al. 2003).

For our fiducial model we assume that the 25 M$_\odot$ progenitor (Woosley et al. 2002) ends up as a stripped pre-SN star with a 8.3-M$_\odot$ helium core, and a 0.3 M$_\odot$ envelope, with a hydrogen mass fraction of 0.5. The adopted pre-SN radius is $R = 10\,R_\odot$ constrained by the pre-explosion Hα luminosity. To construct the stripped pre-SN configuration, we scaled the mass and the radius of the hydrogen envelope of the 25 M$_\odot$ progenitor to the required values. Using a radiation hydrodynamics code (Utrobin 2007; Utrobin et al. 2015), we analysed the outcome of the explosion which is initiated by a supersonic piston applied to the bottom of the stellar envelope at the boundary of the 2.1-M$_\odot$ central core, which is then removed from the computational mass domain and assumed to collapse into a neutron star. We computed a set of SN models with explosion energies of (0.1–1.0) $\times 10^{51}$ erg, ejecta masses of 0.45–2.1 M$_\odot$, and kinetic energies of (0.2–4.5) $\times 10^{50}$ erg. Note that the explosion energies released at the boundary of the collapsing core are in the plausible range for the neutrino-driven explosion mechanism (Janka 2012). The light curves of these models have a very narrow shock break-out peak ($\sim 10^{-4}$ d), a short overall duration ($\sim$10 d) and a luminosity of $<10^{42}$ erg s^{-1} (after the shock break-out peak), while the expansion velocity at the boundary is large ($>10^4$ km s^{-1}). These properties are in agreement with the

absence of broad absorption lines in the spectra which, in turn, suggest a small energy contribution of the intrinsic SN luminosity to the bolometric light curve, and instead support the CS interaction as the dominant source powering the SN luminosity.

The bolometric luminosity powered by the CS interaction is calculated in a thin shell approximation (Chevalier 1982; Chugai 2001). The model suggests that freely expanding SN ejecta collide with dense CSM. The interaction proceeds via forward and reverse shocks with the CDS at the contact boundary between SN and CSM. The CDS radius R_s and velocity v_s are recovered from the numerical solution of the equations of motion and mass conservation. The forward shock velocity is $v_s - v_w$ (v_w is the wind velocity) and the reverse shock velocity is $R/t - v_s$. The post-shock temperature is set by the shock velocity assuming an isothermal ($T_e = T_i$) strong shock, while the post-shock density is set to be four times the pre-shock density. The X-ray luminosity of the jth shock ($j = 1$ for the forward shock and $j = 2$ for the reverse shock) is $L_j = 2\pi R_s^2 v_j^3 \eta_j$, where v_j is the shock velocity, $\eta_j = t/(t + t_{c,j})$ is the cooling efficiency and $t_{c,j}$ is the post-shock cooling time. The optical bolometric luminosity is calculated assuming that the full X-ray luminosity of both shocks is absorbed by the cool material of the CDS, the unshocked SN ejecta and the CSM.

We consider two cases: (i) spherically symmetric CSM with velocities $v = v_0(r/r_0)$ for $r < r_0$ and $v = v_0 = 2000$ km s^{-1} for $r > r_0 \approx 5 \times 10^{15}$ cm and (ii) anisotropic CSM with a dense equatorial disc and a rarefied, more symmetric flow. This latter outflow presumably does not contribute significantly to the interaction luminosity, although it is responsible for the narrow Hα absorption. The equatorial CSM is assumed to have a low expansion velocity: we set it to be 100 km s^{-1} (the result does not depend on the exact value of v_w). The CSM anisotropy is set as the fraction of a sphere occupied by the equatorial CSM, $G = \Omega(r)/4\pi$. This factor multiplied by the luminosity computed for the spherical CSM gives the luminosity in the anisotropic case. Indeed, the luminosity and its temporal evolution constrain the CS density and its radial distribution. We find that the requirement of a rapid deceleration suggests a low-mass and low-energy SN ejecta in order to minimize the ejecta momentum. A search for the best-fitting model in an extended parameter space leads us to conclude that one cannot describe simultaneously the light curve and the low expansion velocity in the framework of a spherically symmetric model. This is the primary reason to invoke an asymmetric CSM. We do not pursue the goal to find the best-fitting model for the CSM using a minimization procedure. Our best-fitting model should be considered rather as a reasonable possibility.

The model light curves and the expansion velocity of the CDS for the isotropic and anisotropic CSM cases are shown in Fig. 21. As parameters for the hydrodynamical model we adopt an ejecta mass $M = 1.15\,M_\odot$ and a kinetic energy $E = 1.6 \times 10^{50}$ erg. The ejecta consist of $0.15\,M_\odot$ of hydrogen and nearly $1.0\,M_\odot$ of helium. The rest of the He core is assumed to fall back, thus possibly making a black hole with a mass of 7–8 $M_\odot$. The SN explosion produces the brief shock break-out peak followed by a short quasi-plateau ($\sim$12 d) with a luminosity of $\sim 10^{41}$ erg s^{-1}. This contributes negligibly to the SN luminosity, which is instead dominated by CS interaction (Fig. 21, panels a and c). The modelled interaction luminosity for both the spherical and the anisotropic CSM well fits the observed light curve (Fig. 21, panels a and c), whereas the expansion velocities of the CDS at late times are quite different: the spherical model predicts deceleration down to 3000 km s^{-1}, while the CDS for the equatorial CSM is decelerated down to 1300 km s^{-1} (Fig. 21, panels b and d). In that respect, the non-spherical model is preferred, given the similarities of the model with the velocity evolution of Hα and the He I lines shown in Fig. 9. The total mass of the non-spherical CSM in the range of $r < 3 \times 10^{16}$ cm is $0.13\,M_\odot$. The geometric factor is $G = 0.02$ at the large radii (Fig. 21d, inset) which corresponds to a polar angle width of the equatorial disc of 23°.

The scenario with an equatorial CSM predicts a double-horn line emitted in the interaction zone. Indeed, at $t > +142$ d the Hα shows Blue and Red bumps with radial velocities of about -1100 and 1550 km s^{-1}, respectively (see Table A4). The velocity and intensity differences between those peaks indicate that the structure of the CSM deviates from axial symmetry.

3.5.3 *Evidence from narrow absorption lines*

The narrow absorptions of the Hα, Hβ and Fe II (multiplet 42) lines are shallow in the higher resolution spectra of days +23 to +26 (see Section 2.4). Moreover, Hα and Hβ have similar relative depths, $A \approx 0.1$. Given a theoretical ratio of optical depths Hβ/Hα = 1/7, the facts that the Hβ and Hα absorptions have similar depths and are both shallow imply that these lines are saturated, but only about 10 per cent of the continuum source is covered by line absorbers. The spherical component of the CSM responsible for the narrow absorptions is therefore clumpy and consists of clouds optically thick in the Hα and Hβ lines embedded in the optically thin intercloud gas. The interaction with the clumpy spherical CSM might contribute to the central (Core) Hα emission component ($t > 142$ d). The fact that this emission component is redshifted by 300–400 km s^{-1} could be attributed to the asymmetry of the CSM in a sense that the far side of the quasi-spherical CSM is more dense and mostly contributes to the Core Hα emission.

3.5.4 *The progenitor scenario*

The dominant role of the continuum originated by the CSM–ejecta interaction and the significant deceleration of the SN ejecta indicate lower ejecta mass and explosion energy than in normal core-collapse SNe. We have shown in the previous section that ejecta with $M_{ej} \approx 1.15\,M_\odot$ and $E \approx 1.6 \times 10^{50}$ erg are consistent with the observations. The low hydrogen mass ($\sim 0.15\,M_\odot$) and the high He I luminosity around day +450 imply that the ejecta are made up primarily of helium ($\sim 0.8\,M_\odot$).

The CSM close to the exploding star has an overall spherical distribution (see Fig. 22), but with some density enhancement in an oblate structure to explain the asymmetric early He I line profiles. The inner radius of the equatorial disc is $r \approx 3 \times 10^{15}$ cm, while its external limit is $>5 \times 10^{17}$ cm (>0.15 pc), since the ejecta are still interacting with the disc at the time of our last observation (+5542 d). The disc is embedded in a more spherically symmetric, clumpy CSM. The mass of the CSM in the anisotropic model, including the inner mostly spherical zone is $0.13\,M_\odot$, within a distance $r < 3 \times 10^{16}$ cm. This value is very similar to the amount of CS mass found in the twin SN 1994aj (Paper I) and about 10 times more than in SN 1996L (Paper II). According to this scenario, and given the progressive quenching of the Hα Core and Red components, we may suppose that both the receding part of the disc and the quasi-symmetric clumpy CSM get shallower and shallower in density with time, or that some obscuring dust is forming mostly inside the shocked ejecta (or a combination of the two).

The presence of dense CSM around the progenitor star of SN 1996al is also supported by the recovery of the progenitor in an

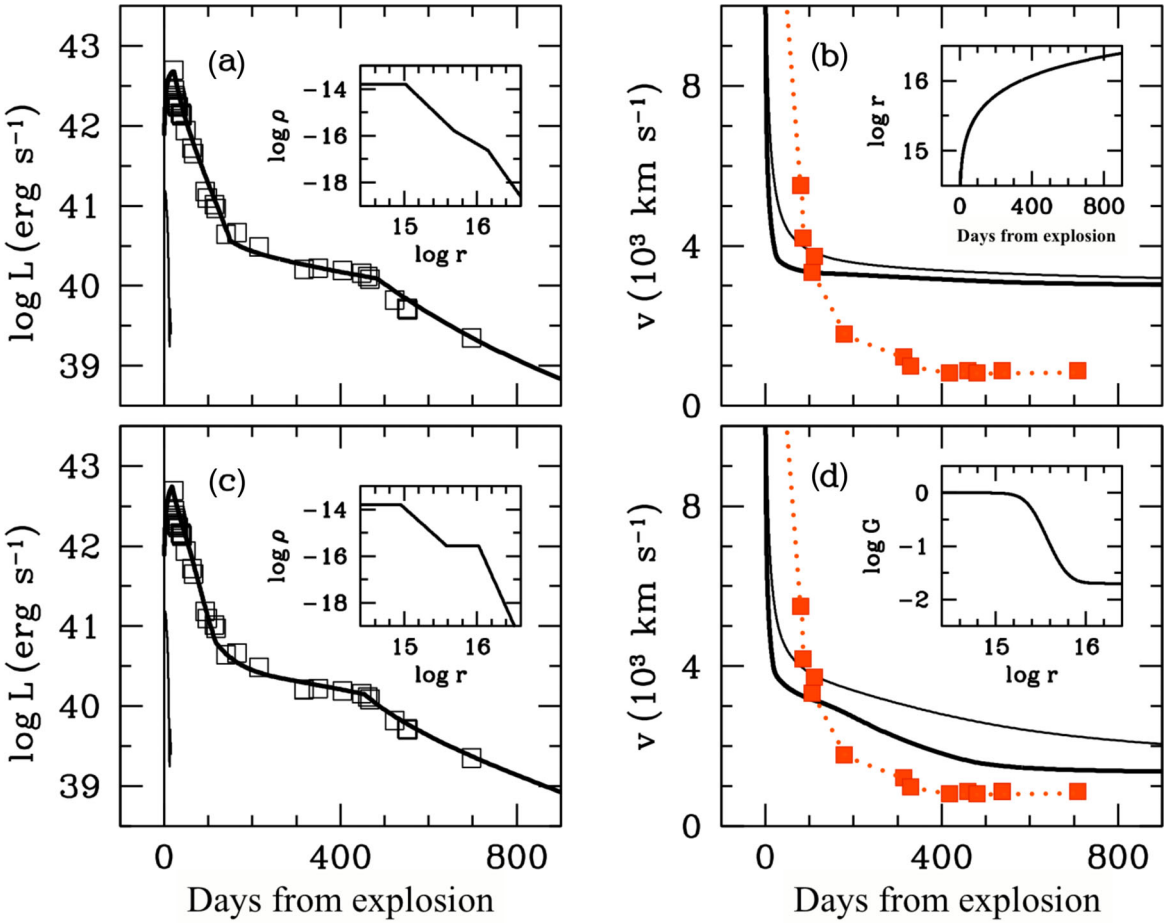

Figure 21. Bolometric light curve and expansion velocity in the CS interaction model. Panel (a): light curves of the fast-evolving dim hydrodynamic model (thin line) and the interaction model (thick line) in the spherical case compared to the observations (open squares). The inset shows the CS density distribution, where ρ and r units are g cm^{-3} and cm, respectively. Panel (b): the CDS velocity (thick line) and the boundary velocity of the unshocked SN ejecta (thin line). For comparison, the observed velocities of the He I 7065 Å are also plotted (filled red squares connected with a dotted red line). The inset shows the CDS radius. Panel (c): the same as in panel (a) but for the non-spherical case. Panel (d): the CDS velocity (thick line) and the boundary velocity of the unshocked SN ejecta in the equatorial plane (thin line). For comparison, the observed velocities of the He I 7065 Å are also plotted (filled red squares connected with a dotted red line). The inset shows the geometric factor describing the angular width of the equatorial disc (see text).

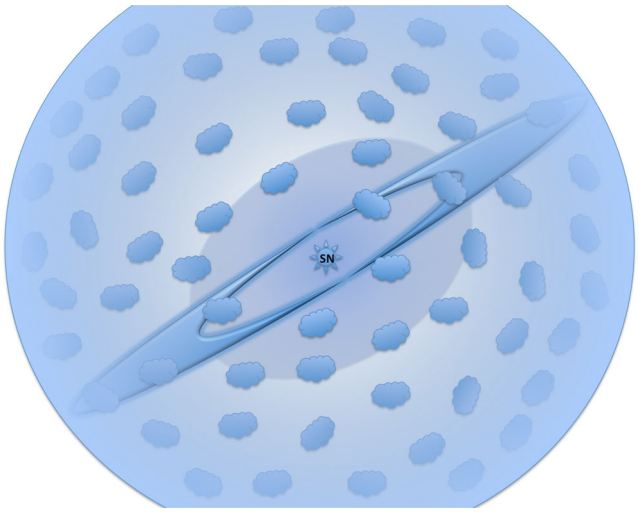

Figure 22. Schematic cartoon of the CSM shape surrounding SN 1996al (not to scale). Line of sight is perpendicular to the figure plane. See text for a description.

archive Hα image, from which a Hα luminosity of log $L_{H\alpha} \sim 37.28$ is derived. This Hα luminosity implies a massive ~25-$M_\odot$ ZAMS progenitor star (see Section 3.1), which has lost almost the entire hydrogen envelope during its evolution.

It is interesting to note that such a highly asymmetric geometric configuration derived for the SN 1996al CSM has been observed around very massive evolved stars such as MN18, and in other blue supergiants (including LBV candidates) of Milky Way and Large Magellanic Cloud (LMC), including the SN 1987A's progenitor (Gvaramadze et al. 2015).

In this scenario, the absence of [O I] 6300–6364-Å emission lines at any phase (see Fig. 23) is naturally explained since most of the oxygen layer has fallen on to the black hole.[5]

[5] It is interesting to note that a similar scenario (low energy, 4×10^{50} erg; massive, 26 $M_\odot$, progenitor; substantial fallback of material on to the collapsed core) has been proposed to explain the physical characteristics of SN 1997D (Turatto et al. 1998; Benetti et al. 2001). However, this high-mass scenario has been questioned by Chugai & Utrobin (2000) who, instead, proposed a low-mass progenitor for SN 1997D. In the case of SN 1996al the key parameter that point towards a high-mass progenitor scenario is the pre-explosion Hα luminosity.

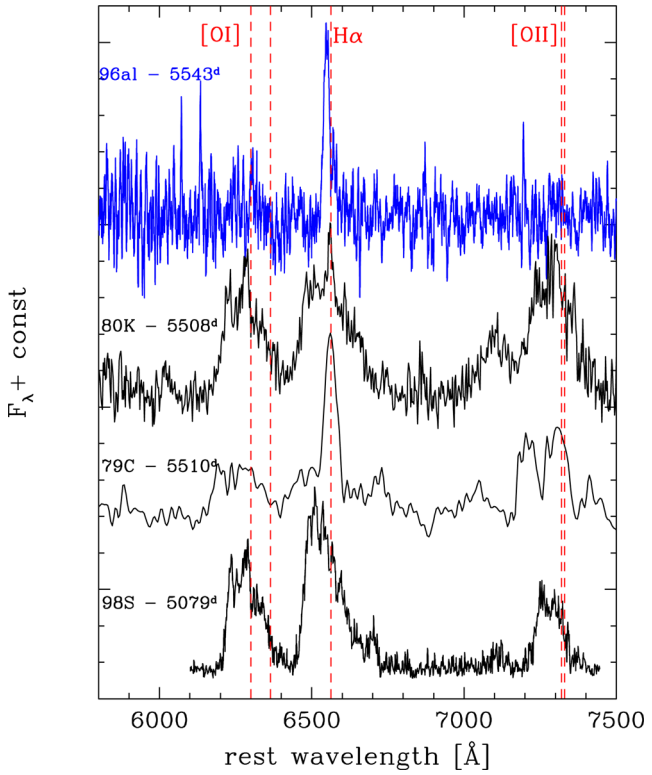

Figure 23. Comparison of spectra taken about 14 yr after explosion of our SNe sample. The SNe 1979C and 1980K spectra are from Fesen et al. (1999), while that of SN 1998S is from Mauerhan & Smith (2012).

4 CONCLUSIONS

Extensive photometric and spectroscopic observations of SN 1996al along 15 yr of its evolution are presented. The light curve indicates that the SN is of Type IIL, reaching peak absolute magnitudes of $M_B \sim -18.6$ and $M_V \sim -18.2$. However, a closer inspection shows that the decline rate changes with time, and this is correlated with significant changes in the spectral appearance. The complex SN evolution is very likely a consequence of the primary role played by the ejecta–CSM interaction during all phases of the SN life.

The spectra obtained soon after the maximum light show narrow P-Cygni Balmer lines superimposed on broader components with asymmetric profiles. In addition, broad and asymmetric He I lines in emission are detected. At these early phases, the broad H component and the He lines form in the same outer region of the ejecta. By day +142, the Hα profile dramatically changes: the narrow emission component disappears, and Hα splits in three components of comparable widths, that remain at constant wavelengths afterward. This composite profile remains visible over 15 yr, although the relative strengths of the three components change with time.

The He lines behave differently. After day +100, they become significantly narrower ($\leq$1000 km s^{-1}) and symmetric, a clear indication that they form in a different region of the ejecta. Later on, between day +300 and +600, they experience a sudden increase in flux. Then, the flux of the He I line decreases again, and by day +700, these lines fade below the detection threshold.

We have also recovered information on the progenitor star by inspecting a pre-explosion archive image in the Hα narrow band. A luminous source is detected at the location of SN 1996al, showing a total Hα luminosity of 1.9×10^{37} erg s^{-1}, which favours a massive (25 $M_\odot$ ZAMS) progenitor star for SN 1996al. This, along with the SN parameters derived by the modelling, suggests that the progenitor was stripped of a large fraction of the hydrogen envelope in the latest stages of its life which ended with the collapse of a 7–8-$M_\odot$ helium core.

The peculiar evolution of the H and He I lines is likely a consequence of the geometry, the non-uniform density profile of the CSM surrounding SN 1996al and the fallback on to the compact remnant. Observational evidences favour a highly structured CS scenario characterized by inner high-density material with oblate structure plus an equatorial ring extended over 0.15 pc, both embedded in a more spherically symmetric, lower-density but clumpy CSM. The total mass of the CSM is modest, being $\gtrsim 0.13$ $M_\odot$ within a distance $\lesssim 3 \times 10^{16}$ cm.

Models show that the luminosity of SN 1996al is best sustained by SN ejecta–CSM interaction. The inferred ejected mass is relatively small ($\sim$1.15 $M_\odot$, $\sim$0.15 $M_\odot$ of which is hydrogen, the residual fraction is helium) and is expelled in a low kinetic energy explosion ($\sim 1.6 \times 10^{50}$ erg). The amount of ejected ^{56}Ni (if any) expelled in the explosion is constrained to be $\lesssim 0.018 M_\odot$. The modest ejecta and ^{56}Ni mass are explained with a massive fallback of material into the compact remnant, producing a 7–8-$M_\odot$ black hole.

ACKNOWLEDGEMENTS

We thank the anonymous referee for very useful comments and suggestions.

We thank T. Augusteijn, M. Birlan, J. F. Le Borgne, S. Covino, P. Rosati and G. C. Van de Steene for giving us part of their telescope time; P. Fouqué for supplying the DENIS photometry; and M. Riello for performing some of the observations.

We are indebted to N. Richardson for providing unpublished spectra of LBVs.

We thank R. McCray and J. Marcaide for helpful discussions and comments on the manuscript.

SB, MT and AP are partially supported by the PRIN-INAF 2014 project Transient Universe: unveiling new types of stellar explosions with PESSTO. VPU is supported by Russian Scientific Foundation grant 14-12-00203. NC thanks the Program of RAS 'Explosions in Astrophysics' for financial support. GP acknowledge support provided by the Millennium Institute of Astrophysics (MAS) through grant IC120009 of the Programa Iniciativa Cientifica Milenio del Ministerio de Economia, Fomento y Turismo de Chile.

This work is based on observations collected at the ESO-La Silla (under programmes ESO no. 151.D-0004, 56.D-0478, 57.D-0534, 58.D-0307, 59.D-0332, 60.D-0415, 61.D-0630, 57.E-0646); and ESO-Paranal (under programmes ESO no. 67.D-0422, 073.D-0670, 080.D-0213, 084.D-0265, 087.D-0693) Observatories.

One spectrum has been collected at the Anglo Australian Observatory by R. Stathakis, B. Schmidt and S. Woodings and retrieved via AAT Archive (http://apm5.ast.cam.ac.uk/arc-bin/wdb/aat_database/observation_log/make).

This research has made use of the NASA/IPAC Extragalactic Database (NED) which is operated by the Jet Propulsion Laboratory, California Institute of Technology, under contract with the National Aeronautics and Space Administration. We have also made use of the Lyon-Meudon Extragalactic Database (LEDA), supplied by the LEDA team at the Centre de Recherche Astronomique de Lyon, Observatoire de Lyon.

REFERENCES

Almog Y., Netzer H., 1989, MNRAS, 238, 57
Aretxaga I., Benetti S., Terlevich R. J., Fabian A. C., Cappellaro E., Turatto M., della Valle M., 1999, MNRAS, 309, 343
Barbon R., Ciatti F., Rosino L., 1982, A&A, 116, 35
Benetti S., Neuhauser R., 1996, IAU Circ., 6438, 1
Benetti S., Cappellaro E., Danziger I. J., Turatto M., Patat F., della Valle M., 1998, MNRAS, 294, 448 (Paper I)
Benetti S., Turatto M., Cappellaro E., Danziger I. J., Mazzali P. A., 1999, MNRAS, 305, 811 (Paper II)
Benetti S. et al., 2001, MNRAS, 322, 361
Branch D., Falk S. W., Uomoto A. K., Wills B. J., McCall M. L., Rybski P., 1981, ApJ, 244, 780
Buonanno R., Buscema G., Corsi C. E., Ferraro I., Iannicola G., 1983, A&A, 126, 278
Buta R. J., 1982, PASP, 94, 578
Caldwell N., Kennicutt R., Phillips A. C., Schommer R. A., 1991, ApJ, 370, 526
Cappellaro E., Danziger I. J., della Valle M., Gouiffes C., Turatto M., 1995, A&A, 293, 723
Cardelli J. A., Clayton G. C., Mathis J. S., 1989, ApJ, 345, 245
Chandrasekhar S., 1960, Radiative Transfer. Dover, New York
Chevalier R. A., 1982, ApJ, 259, 302
Chevalier R. A., Fransson C., 1994, ApJ, 420, 268
Chugai N. N., 1990, SvA, 16, L457
Chugai N. N., 2001, MNRAS, 326, 1448
Chugai N. N., Utrobin V. P., 2000, A&A, 354, 557
Crowther P. A., Lennon D. J., Walborn N. R., 2006, A&A, 446, 279
Danziger I. J., 1988, in Greco M., ed., Results and Perspectives in Particle Physics. Editions Frontieres, Gif sur Yvette, France, p. 3
Dexter J., Kasen D., 2013, ApJ, 772, 30
Doggett J. B., Branch D., 1985, AJ, 90, 2303
Evans R., Benton R., Beaman S., Pogson J., Ryan S., 1996, IAU Circ., 6437, 1
Faran T. et al., 2014, MNRAS, 445, 554
Fassia A. et al., 2000, MNRAS, 318, 1093
Fassia A. et al., 2001, MNRAS, 325, 907
Fesen R. A. et al., 1999, AJ, 117, 725
Freedman W. L. et al., 2001, ApJ, 553, 47
Gvaramadze V. V. et al., 2015, MNRAS, 454, 219
Heger A., Fryer C. L., Woosley S. E., Langer N., Hartmann D. H., 2003, ApJ, 591, 288
Hoekzema N. M., Lamers H. J. G. L. M., van Genderen A. M., 1992, A&A, 257, 118
Humphreys R. M., Martin J. C., 2012, Astrophys. Space Sci. Libr., 384, 1
Humphreys R. M., Lamers H. J. G. L. M., Hoekzema N., Cassatella A., 1989, A&A, 218, L17
Janka H.-T., 2012, Annu. Rev. Nucl. Part. Sci., 62, 407
Karachentsev I. D., Sharina M. E., Huchtmeier W. K., 2000, A&A, 362, 544
Kennicutt R. C., Hodge P. W., 1980, ApJ, 241, 573
Kraan-Korteweg R. C., 1986, A&AS, 66, 255
Landolt A. U., 1992, AJ, 104, 340
Liu Q.-Z., Hu J.-Y., Hang H.-R., Qiu Y.-L., Zhu Z.-X., Qiao Q.-Y., 2000, A&AS, 144, 219
Massey P., 2000, PASP, 112, 144
Mauerhan J., Smith N., 2012, MNRAS, 424, 2659
Oke J. B., 1990, AJ, 99, 1621
Osterbrock D. E., 1989, Astrophysics of Gaseous Nebulae and Active Galactic Nuclei. University Science Books, Mill Valley, CA
Pastorello A. et al., 2010, MNRAS, 408, 181
Pastorello A. et al., 2013, ApJ, 767, 1
Patat F., Barbon R., Cappellaro R., Turatto M., 1994, A&A, 282, 731
Pietrzyński G. et al., 2013, Nature, 495, 76
Richardson N. D., Gies D. R., Morrison N. D., Schaefer G., ten Brummelaar T., Monnier J. D., Parks J. R., 2012, in Drissen L., Robert C., St-Louis N., Moffat A. F. J., eds, ASP Conf. Ser. Vol. 465, Proceedings of a Scientific Meeting in Honor of Anthony F. J. Moffat. Astron. Soc. Pac., San Francisco, p. 160
Schlegel D. J., Finkbeiner D. P., Davis M., 1998, ApJ, 500, 525
Shore S. N., Altner B., Waxin I., 1996, AJ, 112, 2744
Simón-Díaz S., Stasińska G., 2008, MNRAS, 389, 1009
Smartt S. J., 2009, ARA&A, 47, 63
Smith N. et al., 2010, AJ, 139, 1451
Stahl O., Jankovics I., Kovács J., Wolf B., Schmutz W., Kaufer A., Rivinius T., Szeifert T., 2001, A&A, 375, 54
Stetson P. B., 1992, in Worall D. M., Biemesderfer C., Barnes J., eds, ASP Conf. Ser. Vol. 25, Astronomical Data Analysis Software and Systems I. Astron. Soc. Pac., San Francisco, p. 297
Terlevich R. J., 1994, in Clegg R. E. S., Stevens I. R., Meikle W. P. S., eds, Circumstellar Media in the Late Stages of Stellar Evolution. Cambridge Univ. Press, Cambridge, p. 153
Tsvetkov D. Y., 1983, Perem. Zvezdy, 22, 39
Turatto M., Cappellaro E., Danziger I. J., Benetti S., Gouiffes C., della Valle M., 1993, MNRAS, 262, 128
Turatto M. et al., 1998, ApJ, 498, L129
Turatto M., Benetti S., Cappellaro E., 2003, in Leibundgut B., Hillebrandt W., eds, ESO Astrophys. Symp., From Twilight to Highlight: The Physics of Supernovae: Proceedings of the ESO/MPA/MPE Workshop. Springer-Verlag, Berlin, p. 200
Uomoto A., Kirshner R. P., 1986, ApJ, 308, 685
Utrobin V. P., 2007, A&A, 461, 233
Utrobin V. P., Wongwathanarat A., Janka H.-T., Müller E., 2015, A&A, 581, A40
van Genderen A. M., Robijn F. H. A., van Esch B. P. M., Lamers H. J. G., 1991, A&A, 246, 407
Vernet J. et al., 2011, A&A, 536, A105
Walborn N. R., 2012, Astrophys. Space Sci. Libr., 384, 25
Willick J. A., Courteau S., Faber S. M., Burstein D., Dekel A., Strauss M. A., 1997, ApJS, 109, 333
Woosley S. E., Hartmann D., Pinto P. A., 1989, ApJ, 346, 395
Woosley S. E., Heger A., Weaver T. A., 2002, Rev. Mod. Phys., 74, 1015

APPENDIX A

A1 Light curves and spectroscopic log of SN 1996al

Table A1. Optical and NIR photometric measurements for SN 1996al.

Date	MJD	ph (d)[a]	*U*	*B*	*V*	*R*	*I*	*J*	*H*	Tel.	Seeing (arcsec)
1996-07-23	50287.29	22.8	14.27(08)	14.80(05)	14.61(04)	14.37(04)	14.25(04)			Dut	1.3
1996-07-25	50289.32	24.8	14.54(07)	14.98(09)	14.77(03)	14.48(03)	14.36(03)			Dut	2.0
1996-07-26	50290.34	25.8	14.68(05)	15.05(04)	14.81(03)	14.56(03)	14.42(03)			Dut	1.7
1996-07-27	50291.35	26.9	14.76(05)	15.13(04)	14.90(03)	14.62(03)	14.49(03)			Dut	2.4
1996-07-28	50292.32	27.8	14.88(05)	15.19(04)	14.96(03)	14.69(03)	14.56(02)			Dut	1.7
1996-07-29	50293.33	28.8	14.96(04)	15.26(03)	15.01(04)	14.72(03)	14.60(04)			Dut	1.6
1996-07-29	50293.40	28.9						14.27(05)		Den	–
1996-07-30	50294.40	29.9	15.03(09)	15.34(05)	15.03(02)	14.75(04)	14.62(02)			Dut	1.4
1996-08-01	50296.31	31.8	15.00(08)	15.36(05)	15.11(02)	14.81(03)	14.70(02)			Dut	2.2
1996-08-06	50301.30	36.8	15.31(09)	15.55(04)	15.25(03)	14.95(03)	14.83(03)			Dut	1.5
1996-08-07	50302.28	37.8	15.32(07)	15.57(04)	15.28(03)	14.94(03)	14.82(03)			Dut	2.3
1996-08-07	50302.43	37.9			15.29(03)					EF1	1.5
1996-08-08	50303.43	38.9			15.26(02)					EF1	2.4
1996-08-09	50304.43	39.9			15.27(03)					EF1	1.9
1996-08-10	50305.27	40.8			15.27(03)		14.83(04)			Dut	1.4
1996-08-10	50305.43	40.9			15.31(03)	14.95(02)				EF1	1.4
1996-08-18	50313.35	48.9	16.09(05)	16.22(03)	15.79(03)	15.41(03)	15.29(02)			Dut	2.3
1996-09-01	50327.37	62.9			16.30(03)					EF1	1.5
1996-09-05	50331.33	66.8	17.11(06)	17.14(05)	16.48(03)	16.02(04)	15.86(03)			EF2	2.1
1996-10-01	50357.27	92.8		18.33(05)	17.76(04)	17.29(03)	17.13(03)			DF	1.5
1996-10-08	50363.12	98.6	18.34(06)	18.50(05)	17.99(03)	17.50(03)	17.35(03)			EF2	2.5
1996-10-24	50379.06	114.6	18.63(08)	18.65(07)	18.12(04)	17.64(05)	17.47(04)			Dut	2.5
1996-10-28	50383.13	118.6	18.71(07)	18.78(05)	18.24(04)	17.75(04)	17.60(04)			Dut	1.4
1996-11-18	50405.02	140.5			19.22(04)					EF1	1.4
1996-11-18	50405.08	140.6	19.44(06)	19.66(05)	19.24(04)	18.46(04)	18.36(04)			Dut	1.5
1996-12-01[b]	50418.15	153.6						18.45(20)	18.33(20)	IR2	0.7
1996-12-13	50430.00	165.5		19.56(05)	18.97(03)	18.39(03)	18.25(03)			EF2	2.0
1997-02-01	50480.05	215.6			19.68(05)	18.85(04)				Dut	1.5
1997-05-13	50581.41	316.9	20.92(09)	20.85(05)	20.39(05)	19.43(05)	19.69(04)			EF2	1.5
1997-05-14	50582.35	317.9			20.41(06)	19.46(06)				EF2	1.4
1997-06-15	50614.54	350.0			20.20(06)	19.34(06)				DF	1.8
1997-08-09	50669.40	404.9		20.71(09)	20.26(08)	19.46(06)	19.83(06)			DF	1.7
1997-09-16	50708.00	443.5						19.05(20)	19.11(20)	IR2	1.2
1997-09-17	50709.00	444.5						18.92(20)	19.08(20)	IR2	1.1
1997-09-22	50713.17	448.7	21.01(20)	20.80(10)	20.43(08)	19.52(09)	19.92(08)			EF2	1.4
1997-09-23	50714.13	449.6				19.66(10)				EF2	1.3
1997-10-06	50726.07	461.6		20.75(10)	20.54(09)	19.72(08)	20.05(08)			Dut	1.3
1997-10-12	50732.02	467.5			20.66(08)	19.74(07)				DF	1.7
1997-11-17	50769.70	505.2						19.54(30)		IR2	0.9
1997-12-05	50787.08	522.6		21.59(10)	21.38(07)	20.31(07)	20.69(08)			DF	1.4
1998-01-02	50815.08	550.6			21.58(20)	20.59(10)	20.90(10)			Dut	1.5
1998-01-03	50816.18	551.6			21.56(10)					Dut	1.6
1998-01-04	50817.10	552.6			21.67(15)	20.54(10)				Dut	1.5
1998-01-05	50818.05	553.6						20.40(40)		IR2	0.7
1998-05-29	50962.42	697.9		22.83(20)	22.51(10)	21.38(10)				EF2a	1.4
1998-05-30	50963.40	698.9				21.39(10)				EF2a	1.0
1998-07-05	50999.41	734.9				21.48(10)				Dut	1.8
1998-09-12	51068.80	804.3				21.99(10)				EF2a	1.1

Notes. [a]Epoch relative to V_{max} occurred on MJD = 50265. [b]For this epoch we give also $K = 17.68(20)$.
Dut = Dutch+CCD camera; pixel scale = 0.44 arcsec per pixel. Den = ESO1.0m+DENIS; pixel scale = 3 arcsec per pixel. EF1 = ESO3.6m+EFOSC1; pixel scale = 0.61 arcsec per pixel. EF2 = MPI2.2m+EFOSC2; pixel scale = 0.34 arcsec per pixel. DF = D1.54m+DFOSC; pixel scale = 0.39 arcsec per pixel. IR2 = MPI2.2m+IRAC2; pixel scale = 0.28 arcsec per pixel. EF2a = ESO3.6m+EFOSC2; pixel scale = 0.157 arcsec per pixel.

A2 Spectral line parameters of SN 1996al

Table A2. Spectroscopic observations of SN 1996al.

Date	MJD	Phase[a] (d)	Range (Å)	Tel.[b]	Res. (Å)
1996-07-23	50287.54	23	4400–7000	B&C	4
1996-07-24	50288.39	24	4400–7000	B&C	4
1996-07-25	50289.34	25	4400–7000	B&C	4
1996-07-26	50290.34	26	4400–7000	B&C	4
1996-07-29	50293.35	29	4030–9720	B&C	9
1996-07-30	50294.34	30	4030–9720	B&C	9
1996-07-31	50295.35	31	4030–9720	B&C	9
1996-08-01	50296.38	32	4030–9720	B&C	9
1996-08-07	50302.44	38	3740–6930	EF1	16
1996-08-08	50303.44	39	3740–6930	EF1	16
1996-08-09	50304.43	40	3740–6930	EF1	16
1996-08-10	50305.43	41	3740–9890	EF1	16
1996-08-12	50307.41	43	4940–6930	B&C	3
1996-08-22	50317.16	53	3490–11 080	B&C	13
1996-09-01	50327.38	63	3730–6910	EF1	16
1996-09-05	50331.38	67	3200–9250	EF2	10
1996-09-10	50336.15	72	3520–10 320	B&C	13
1996-10-01	50357.29	93	3300–9050	DF	11
1996-10-07	50363.30	99	5160–9270	EF2	11
1996-10-07	50363.30	99	3430–10 080	EF2	25
1996-10-09	50365.51	101	5430–8890	RGO	8
1996-11-19	50406.03	142	3730–6910	EF1	16
1996-12-13	50430.12	166	3840–7990	EF2	12
1997-04-30	50568.40	304	3600–9600	B&C	12
1997-05-14	50582.35	318	5220–9250	EF2	11
1997-08-10	50670.19	406	5100–10 170	DF	12
1997-09-22	50713.73	449	3500–9300	EF2	10
1997-10-08	50729.07	465	3350–10 040	B&C	12
1997-10-11	50732.07	468	3400–8740	DF	12
1997-12-05	50787.12	523	3500–8990	DF	11
1998-05-29	50962.91	698	3380–7500	EF2a	18
1998-09-12	51068.33	804	3320–7500	EF2a	18
2001-07-27	52117.28	1853	4180–8180	FOR1	14
2002-06-16	52441.31	2177	4090–9630	FOR1	10
2004-07-23	53209.30	2944	4220–9630	FOR2	10
2007-12-08	54442.04	4178	3900–9600	FOR2	10
2009-10-11	55115.04	4850	3500–24 000	XS	1,0.8,2.8
2011-09-03	55807.07	5542	3500–24 000	XS	1,0.8,2.8

Notes. [a]Relative to the estimated epoch of V maximum (MJD = 50265). [b]See note to Table A1 for telescope coding plus: B&C = ESO1.52m+B&C; RGO = AAT+RGO; FOR1 = ESO-VLT+FORS1; FOR2 = ESO-VLT+FORS2; XS = ESO-VLT+XShooter. The resolutions of XS refer to the three arms at 5000, 6000and 15 000 Å, respectively.

Table A3. Spectral line parameters as derived from spectra of SN 1996al up to 100 d.

Phase (d)		Hα			He I 6678	He I 7065
		$(\mathrm{Em})_b$	$(\mathrm{Ab})_n$	$(\mathrm{Em})_n$		
	λ_c (Å)	6564	6556	6566		
+23	FWHM;$V_{l_0}^{\mathrm{blue}}$ (km s^{-1})	6500;12 200	1050	400		
	ϕ^a	372	−35	93		
	λ_c (Å)	6568	6557	6566		
+24	FWHM;$V_{l_0}^{\mathrm{blue}}$ (km s^{-1})	6600;12 700	930	390		
	ϕ^a	477	−41	107		

Table A3 – *continued*

Phase (d)		Hα			He I 6678	He I 7065
		$(Em)_b$	$(Ab)_n$	$(Em)_n$		
	λ_c (Å)	6567	6556	6565		
+25	FWHM;$V_{I_0}^{blue}$ (km s^{-1})	6600;12 800	970	380		
	ϕ^a	482	−43	103		
	λ_c (Å)	6566	6556	6566		
+26	FWHM;$V_{I_0}^{blue}$ (km s^{-1})	7000;12 700	990	410		
	ϕ^a	513	−40	99		
	λ_c (Å)	6566	6551	6565		7065
+29	FWHM;$V_{I_0}^{blue}$ (km s^{-1})	6800;10 300	1030	290		10 600
	ϕ^a	560	−29	75		70
	λ_c (Å)	6565	6551	6565		7065
+30	FWHM;$V_{I_0}^{blue}$ (km s^{-1})	6900;12 600	1020	350		10 800
	ϕ^a	546	−30	73		59
	λ_c (Å)	6565	6551	6565		7065
+31	FWHM;$V_{I_0}^{blue}$ (km s^{-1})	6400;13 100	970	310		9600
	ϕ^a	446	−25	54		59
	λ_c (Å)	6565	6550	6565		7065
+32	FWHM;$V_{I_0}^{blue}$ (km s^{-1})	6500;11900	1020	300		10 200
	ϕ^a	482	-27	54		64
	λ_c (Å)	6572	6554	6565		
+38	FWHM;$V_{I_0}^{blue}$ (km s^{-1})	6300;12 200	550	450		
	ϕ^a	503	−32	71		
	λ_c (Å)	6567	6553	6566		
+39	FWHM;$V_{I_0}^{blue}$ (km s^{-1})	5400;11 500	940	680		
	ϕ^a	471	−37	41		
	λ_c (Å)	6565	6548	6563		7065
+40	FWHM;$V_{I_0}^{blue}$ (km s^{-1})	5800;11 200	580	620		10 600
	ϕ^a	523	−26	39		55
	λ_c (Å)	6568	6549	6567		
+41	FWHM;$V_{I_0}^{blue}$ (km s^{-1})	5600;12 000	530	680		
	ϕ^a	511	−21	33		
	λ_c (Å)	6569	6557	6566	6699	
+43	FWHM;$V_{I_0}^{blue}$ (km s^{-1})	5700;11 800	930	470	5100	
	ϕ^a	440	−36	51	29	
	λ_c (Å)	6568	6555	6565	6712	7035
+53	FWHM;$V_{I_0}^{blue}$ (km s^{-1})	5700;10 200	870	860	3600	10 200
	ϕ^a	209	−30	66	22	37
	λ_c (Å)	6570	6556	6565	6699	
+63	FWHM;$V_{I_0}^{blue}$ (km s^{-1})	5050;11 000	810	940	3300	
	ϕ^a	169	−28	63	16	
	λ_c (Å)	6570	6557	6566	6700	7067
+67	FWHM;$V_{I_0}^{blue}$ (km s^{-1})	4700;11 100	850	650	3250	5500
	ϕ^a	148	−23	38	11	13
	λ_c (Å)	6568	6558	6567	6687	7059
+72	FWHM;$V_{I_0}^{blue}$ (km s^{-1})	4400;10 200	1000	560	3700	4200
	ϕ^a	123	−18	28	16	11
	λ_c (Å)	6563	6560	6566	6673	7065
+93	FWHM;$V_{I_0}^{blue}$ (km s^{-1})	3500;8700	430	230	3300	3300
	ϕ^a	82	−10	11	7	6
	λ_c (Å)	6562	6557	6565	6667	7061
+99	FWHM;$V_{I_0}^{blue}$ (km s^{-1})	3200;10 400	570	460	3300	3700
	ϕ^a	85	−8	6	9	6
	λ_c (Å)	6562	6554	6564	6673	
+101	FWHM;$V_{I_0}^{blue}$ (km s^{-1})	3250;10 600	200:	450	3600	
	ϕ^a	90	−7	3	95	

Notes. [a]In units of $\times$ 10^{-15} erg s^{-1} cm^{-2}; not corrected for reddening.
Hα broad component better fitted with Lorenztians up to phase +43d; after this phase they are better fitted with Gaussians. He I lines always fitted with Gaussians. The velocities have been deconvolved for spectral resolution of each spectrum (see Table A2). Estimated errors: wavelength position: $\sim\pm$ 1 Å for narrow lines; $\lesssim\pm$10 Å for broad lines; FWHM: $\sim\pm$ 90 km s^{-1} for the narrow lines, $\lesssim\pm$500 km s^{-1} for broad lines; ϕ: $\sim$ 1–2 per cent for narrow lines, $\lesssim$ 10 per cent for broad lines.

Table A4. Spectral line parameters as derived from spectra of SN 1996al observed after 100 d.

Phase (d)		Hα			He I 6678	He I 7065
		B_{comp}	C_{comp}	R_{comp}		
	λ_c (Å)	6539	6569	6597	6656	
+142	FWHM;$V_{I_0}^{blue}$ (km s^{-1})	850;7800	950	970	4600	
	ϕ^a	30	26	9	3	
	λ_c (Å)	6542	6570	6595	6678	7071
+166	FWHM;$V_{I_0}^{blue}$ (km s^{-1})	730;6130	680	1340	2500	1800
	ϕ^a	30	21	17	4	3
	λ_c (Å)	6542	6570	6594	6685	7064
+304	FWHM;$V_{I_0}^{blue}$ (km s^{-1})	690;3900	800	630	1950	1200
	ϕ^a	11	11	6	1.5	1.3
	λ_c (Å)	6542	6569	6593	6679	7066
+318	FWHM;$V_{I_0}^{blue}$ (km s^{-1})	580;3800	880	670	1100	950
	ϕ^a	12	16	7	1.0	1.5
	λ_c (Å)	6546	6573	6595	6684	7070
+406	FWHM;$V_{I_0}^{blue}$ (km s^{-1})	550;3400	860	680	930	800
	ϕ^a	8	15	7	3.1	4.5
	λ_c (Å)	6544	6570	6592	6680	7068
+449	FWHM;$V_{I_0}^{blue}$ (km s^{-1})	510;3200	920	650	850	830
	ϕ^a	7	16	7	3.1	5.2
	λ_c (Å)	6545	6571	6592	6681	7068
+468	FWHM;$V_{I_0}^{blue}$ (km s^{-1})	520,2700	1050	720	950	800
	ϕ^a	5.5	13	7	2.3	3.7
	λ_c (Å)	6546	6572	6593	6682	7071
+523	FWHM;$V_{I_0}^{blue}$ (km s^{-1})	520;2400	930	580	980	860
	ϕ^a	5	9	4	0.9	1.6
	λ_c (Å)	6549	6574	6597	6676	7071
+698	FWHM;$V_{I_0}^{blue}$ (km s^{-1})	640;2100	860	630	780	860
	ϕ^a	2.3	2.2	1.4	0.1:	0.2:
	λ_c (Å)	6546	6573	6598		
+804	FWHM;$V_{I_0}^{blue}$ (km s^{-1})	640;1600	1090	720		
	ϕ^a	1.0	1.5	0.8		
	λ_c (Å)	6549	6577	6596		
+1853	FWHM;$V_{I_0}^{blue}$ (km s^{-1})	640;1500	820	<630		
	ϕ^a	0.9	0.6	0.2		
	λ_c (Å)	6550	6577	6594		
+2177	FWHM;$V_{I_0}^{blue}$ (km s^{-1})	960;1700	590	590		
	ϕ^a	0.25	0.05	0.03		
	λ_c (Å)	6552	6577	6593		
+2944	FWHM;$V_{I_0}^{blue}$ (km s^{-1})	770;2400	680	630		
	ϕ^a	0.10	0.02	0.01		
	λ_c (Å)	6551	6577	6593		
+4178	FWHM;$V_{I_0}^{blue}$ (km s^{-1})	680;2200	680	630		
	ϕ^a	0.13	0.02	0.006		
	λ_c (Å)	6552	6582	6599		
+4850	FWHM;$V_{I_0}^{blue}$ (km s^{-1})	960;1300	680	180		
	ϕ^a	0.13	0.03	0.01		
	λ_c (Å)	6552	6575	6585		
+5542	FWHM;$V_{I_0}^{blue}$ (km s^{-1})	1000;1500	320	140		
	ϕ^a	0.12	0.02	0.01		

Notes. [a]In units of $\times$ 10^{-15} erg s^{-1} cm^{-2}; not corrected for reddening.
Hα components better fitted with Lorenztians up to phase +523 d; after this phase the Hα components are better fitted with Gaussians. He I lines always fitted with Gaussians. The FWHMs have been deconvolved for spectral resolution of each spectrum (see Table A2). Estimated errors – wavelength position: about ±1 Å for narrow lines, up to about ±10 Å for broad lines; FWHM: about ±90 km s^{-1} for the narrow lines, up to about ±500 km s^{-1} for the broadest lines; ϕ: about 1–2 per cent for narrow lines, up to ∼10 per cent for the broad lines.

This paper has been typeset from a TEX/LATEX file prepared by the author.